

Exploring Biginelli-based scaffolds as A_{2B} adenosine receptor antagonists: Unveiling novel structure-activity relationship trends, lead compounds, and potent colorectal anticancer agents

Rubén Prieto-Díaz^{a,b,1}, Hugo Fojo-Carballo^{a,b,1}, Maria Majellaro^{a,b,*}, Tana Tandarić^c, Jhonny Azuaje^{a,b}, José Brea^{d,e,**}, María I. Loza^{d,e}, Jorge Barbazán^{f,***}, Glòria Salort^{g,h,i}, Meera Chotalia^{a,b}, Iván Rodríguez-Pampín^{a,b}, Ana Mallo-Abreu^{a,b}, M. Rita Paleo^{a,b}, Xerardo García-Mera^b, Francisco Ciruela^{g,h}, Hugo Gutiérrez-de-Terán^{c,***}, Eddy Sotelo^{a,b,*}

^a Centro Singular de Investigación en Química Biolóxica e Materiais Moleculares (CiQUS), Universidade de Santiago de Compostela, Santiago de Compostela 15782, Spain

^b Departamento de Química Orgánica, Facultade de Farmacia, Universidade de Santiago de Compostela, Santiago de Compostela 15782, Spain

^c Science for Life Laboratory, Department of Cell and Molecular Biology, Uppsala University, Biomedical Centre, Uppsala 75124, Sweden

^d Centro Singular de Investigación en Medicina Molecular y Enfermedades Crónicas (CiMUS), Universidade de Santiago de Compostela, Santiago de Compostela 15782, Spain

^e Departamento de Farmacología, Farmacia e Tecnoloxía Farmacéutica, Facultade de Farmacia, Universidade de Santiago de Compostela, Santiago de Compostela 15782, Spain

^f Grupo de Oncología Médica Traslacional (ONCOMET), Instituto de Investigación Sanitaria, Santiago de Compostela (IDIS), Hospital Universitario de Santiago de Compostela (SERGAS), Santiago de Compostela 15706, Spain

^g Unidad de Farmacología, Departamento de Patología y Terapéutica Experimental, Facultad de Medicina y Ciencias de la Salud, Instituto de Neurociencia, Universitat de Barcelona, L'Hospitalet de Llobregat 08907, Spain

^h Neuropharmacology and Pain Group, Neuroscience Program, Institut d'Investigació Biomèdica de Bellvitge, IDIBELL, L'Hospitalet de Llobregat 08907, Spain

ⁱ Laboratorio de Neurofarmacología, Institut Universitari d'Investigació en Ciències de la Salut (IUNICS), Institut d'investigació Sanitària Illes Balears (IdISBa), University of the Balearic Islands, Palma de Mallorca 07122, Spain

ARTICLE INFO

Keywords:

A_{2B} adenosine receptor
Colorectal cancer
Biginelli reaction

ABSTRACT

Antagonists of the A_{2B} adenosine receptor have recently emerged as targeted anticancer agents and immune checkpoint inhibitors within the realm of cancer immunotherapy. This study presents a comprehensive evaluation of novel Biginelli-assembled pyrimidine chemotypes, including mono-, bi-, and tricyclic derivatives, as A_{2B}AR antagonists. We conducted a comprehensive examination of the adenosinergic profile (both binding and functional) of a large compound library consisting of 168 compounds. This approach unveiled original lead compounds and enabled the identification of novel structure-activity relationship (SAR) trends, which were supported by extensive computational studies, including quantum mechanical calculations and free energy perturbation (FEP) analysis. In total, 25 molecules showed attractive affinity ($K_i < 100$ nM) and outstanding selectivity for A_{2B}AR. From these, five molecules corresponding to the new benzothiazole scaffold were below the $K_i < 10$ nM threshold, in addition to a novel dual A_{2A}/A_{2B} antagonist. The most potent compounds, and the dual antagonist, showed enantiospecific recognition in the A_{2B}AR. Two A_{2B}AR selective antagonists and the dual

Abbreviations: ARs, Adenosine receptors; HA2BR, human A2B adenosine receptors; HA2AR, human A2A adenosine receptors; CAFs, Cancer Associated Fibroblasts; CHO cells, Chinese Hamster Ovary cells; C-AMP, Cyclic adenosine monophosphate; FEP, Free energy perturbation; PDB, Protein Data Bank; SAR, structure-activity relationships; SEM, Standard error of the mean; SCAAS, surface constrained all-atom solvent; SMD, Solvation Model Density.

* Corresponding authors at: Centro Singular de Investigación en Química Biolóxica e Materiais Moleculares (CiQUS), Universidade de Santiago de Compostela, Santiago de Compostela 15782, Spain.

** Corresponding author at: Centro Singular de Investigación en Medicina Molecular y Enfermedades Crónicas (CiMUS), Universidade de Santiago de Compostela, Santiago de Compostela 15782, Spain.

*** Corresponding authors.

E-mail addresses: ma.majellaro@usc.es (M. Majellaro), pepo.brea@usc.es (J. Brea), jorge.barbazan.garcia@sergas.es (J. Barbazán), hugo.gutierrez@icm.uu.se (H. Gutiérrez-de-Terán), e.sotelo@usc.es (E. Sotelo).

¹ These authors contributed equally to this work.

<https://doi.org/10.1016/j.bioph.2024.116345>

Received 18 December 2023; Received in revised form 19 February 2024; Accepted 23 February 2024

Available online 5 March 2024

0753-3322/© 2024 The Author(s). Published by Elsevier Masson SAS. This is an open access article under the CC BY-NC-ND license (<http://creativecommons.org/licenses/by-nc-nd/4.0/>).

$A_{2A}AR/A_{2B}AR$ antagonist reported in this study were assessed for their impact on colorectal cancer cell lines. The results revealed a significant and dose-dependent reduction in cell proliferation. Notably, the $A_{2B}AR$ antagonists exhibited remarkable specificity, as they did not impede the proliferation of non-tumoral cell lines. These findings support the efficacy and potential that $A_{2B}AR$ antagonists as valuable candidates for cancer therapy, but also that they can effectively complement strategies involving $A_{2A}AR$ antagonism in the context of immune checkpoint inhibition.

1. Introduction

Adenosine (Ado) is a signaling nucleoside involved in various biochemical processes in mammalian cells [1]. It is released from cells or generated extracellularly by enzymes that are part of the purinergic signaling pathway [1]. Ado modulates energy transfer, signal transduction, inflammation, immunity, and the sleep-wake cycle, playing a pivotal role in these processes. Although its extracellular concentration is usually low, it can increase rapidly in response to stress, injury, hypoxia, or inflammation, thereby providing tissue protection. Ado acts through four rhodopsin-like G protein-coupled receptors (A_1AR , $A_{2A}AR$, $A_{2B}AR$, and A_3AR), each possessing unique characteristics and long sought as drug targets [2,3]. Initially considered less significant, the $A_{2B}AR$ subtype is now recognized for its activation under pathological conditions [4]. As a result, it has recently garnered attention for its potential in several therapeutic applications, including inflammation, diabetes, pain, asthma, Alzheimer's disease, and cancer [5–9]. Recently, $A_{2B}AR$ antagonists have demonstrated their potent antiproliferative, anti-angiogenic, and antimetastatic effects [10,11]. Moreover, a recent study has unveiled the promising role of $A_{2B}AR$ antagonism in reactivating the immune system, specifically within the context of cancer immunotherapy [8]. Although recent studies suggest the formation of heteromeric complexes between $A_{2A}AR$ and $A_{2B}AR$ [12], the mechanism

behind the synergistic effect of dual $A_{2A}AR/A_{2B}AR$ antagonists remains unclear.

The discovery and optimization of $A_{2B}AR$ antagonists has been driven by naturally occurring xanthine derivatives, including caffeine and theophylline. Over the years, this led to the identification of derivatives with optimal affinity and selectivity for $A_{2B}AR$ (Fig. 1, compounds 1–4) [13–15]. However, the challenging physicochemical properties and pharmacokinetic profiles of those derivatives have limited their advancement in drug development [13]. Consequently, our recent efforts, along with those of others, have focused on optimizing non-xanthine $A_{2B}AR$ antagonists. Specifically, we have concentrated on pyrimidine-based ligands that offer structural novelty, high affinity, selectivity, and synthetic feasibility (Fig. 1, compounds 5–10) [10, 16–20]. Among these, the chemotypes in compounds 7–10 contain a chiral center within the heterocyclic core, providing a unique structural element compared to planar $A_{2B}AR$ antagonists. The separation of racemates allowed the identification of potent and selective antagonists with enantiospecific recognition at $A_{2B}AR$ [10,18–20], and more recently, at $A_{2A}AR$ [18] as well.

In the framework of our optimization program of non-xanthine $A_{2B}AR$ antagonists as promising anticancer agents [8,10], we here present an exhaustive exploration of the adenosinergic profile of diverse pyrimidine-based scaffolds inspired by compounds 7–10 (Fig. 1) [17,19],

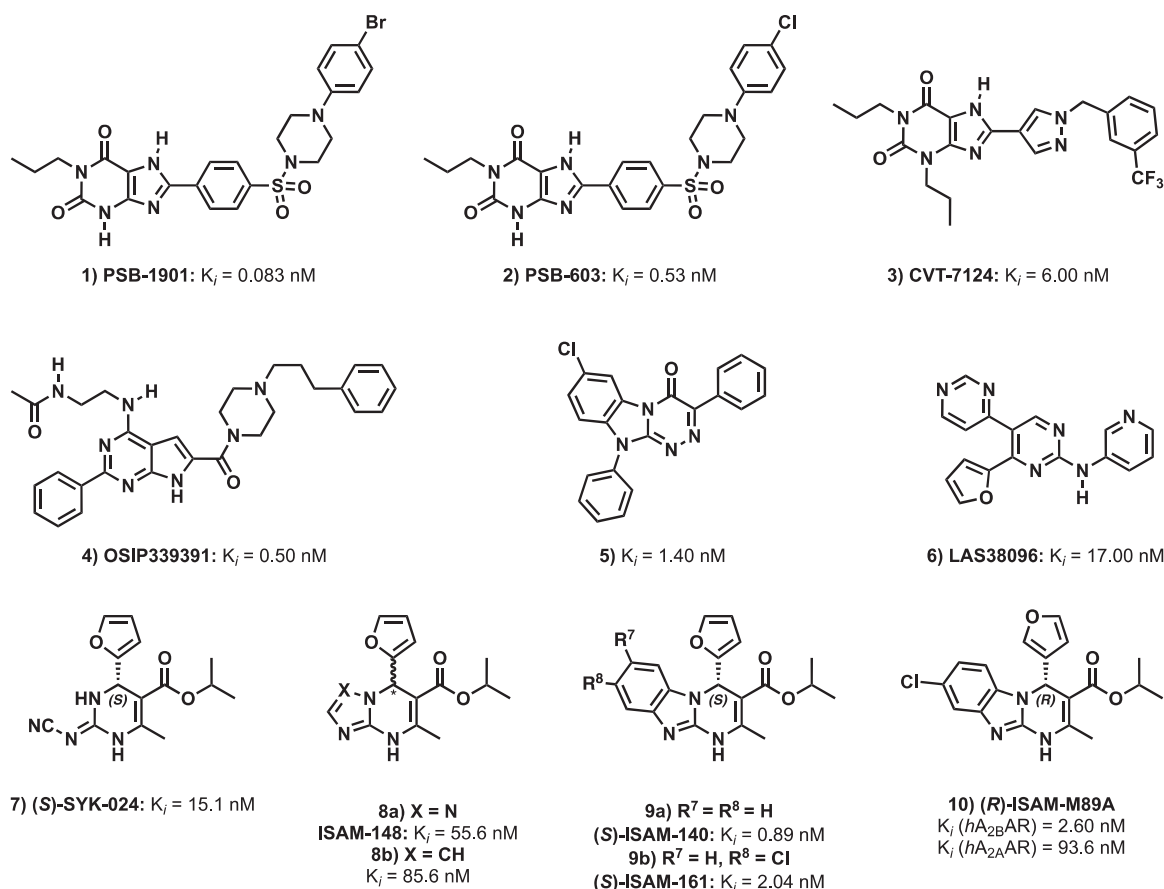


Fig. 1. Structure of representative potent and selective $A_{2B}AR$ antagonists (1–9) and a dual $A_{2A}/A_{2B}AR$ antagonist (10).

thereby unveiling novel SAR trends and identifying unique chemotypes with excellent pharmacodynamic profiles. The design and synthesis of this collection, comprising 168 novel mono-, bi- and tricyclic ligands (Fig. 2, series I-XXI), was inspired by the exploratory capabilities of the Biginelli reaction, complemented by prior SAR data and computational models from early series. Among these new derivatives, benzo[4,5]thiazolo[3,2-*a*]pyrimidines (series XIX, XX, and XXI) stand out as particularly compelling ligands. Apart from their high affinity and selective A_{2B}AR antagonistic profile, they exhibit differential structural features, thereby revealing novel binding modes and structure-activity relationship (SAR) trends. This study further confirms our model for the enantiospecific A_{2B}AR recognition of the pentagonal ring at position 4, and the antagonist profile of the most promising compounds. Three of the lead compounds here developed were selected to investigate the effect of A_{2B}AR antagonism on colorectal cancer cell lines and cancer-associated fibroblasts (CAFs), confirming a notable reduction in cell viability attributed to decreased cell division and an increased apoptosis, specifically in tumour cells, without affecting other non-tumoral cells of the tumour microenvironment.

2. Material and methods

2.1. Chemistry

All starting materials, reagents and solvents were purchased and used without further purification. After extraction from aqueous phases, the organic solvents were dried over anhydrous magnesium sulphate. The reactions were monitored by thin-layer chromatography (TLC) on 2.5 mm Merck silica gel GF 254 strips, and the purified compounds each showed a single spot. Unless stated otherwise, UV light and/or *p*-anisaldehyde were used to detect compounds. The Biginelli reactions were performed in coated Kimble vials on a PLS (6×4) Organic Synthesizer with orbital stirring or Anton Paar Microwave Synthesis Reactor. The purity and identity of all tested compounds were established by a combination of HPLC, mass spectrometry and NMR spectroscopy as described in the Supporting Information. Purification of isolated products was carried out by column chromatography (Kieselgel 0.040–0.063 mm, E. Merck) or medium pressure liquid chromatography (MPLC) on a Combi Flash Companion (Teledyne ISCO) with RediSep pre-packed normal-phase silica gel (35–60 μm) columns followed by recrystallization. Melting points were determined on a Stuart Scientific melting point apparatus and are uncorrected.

The NMR spectra were recorded on Bruker AM300 and XM500 spectrometers. Chemical shifts are given as δ values against tetramethylsilane as internal standard and *J* values are given in Hz. Mass spectra were obtained on a Varian MAT-711 instrument. High-resolution mass spectra were obtained on an Autospec Micromass spectrometer. Analytical HPLC was performed on a Water Breeze™ 2 system (binary pump 1525, detector UV/Visible 2489, 7725i Manual Injector Kit 1500 Series) using a Luna 5 μm Silica (2) 100 Å, LC Column 150 × 4.6 mm column with gradient elution using the mobile phases dichloromethane, isopropanol, and a flow rate of 1 ml/min. The purity of all tested compounds was determined to be >95%. The chiral resolution was performed using a Water Breeze™ 2 (binary pump 1525, detector UV/Visible 2489, 7725i Manual Injector Kit 1500 Series). All enantiomers were separated using a 250 mm × 20 mm Chiralpak® 5 μm IE-3 (DAICEL). All single stereoisomers were isolated and their stereochemical purity analysed by chiral HPLC (>97% for each stereoisomer) and then characterized by NMR in CDCl₃. CD spectra were recorded on a Jasco-815 system equipped with a Peltier-type thermostatic accessory (CDF-426S, Jasco). Measurements were carried out at 20 °C using a 1-mm quartz cell in a volume of 300–350 ml. Compounds (0.1 mg) were dissolved in MeOH (1.0 ml). The instrument settings were bandwidth, 1.0 nm; data pitch, 1.0 nm; speed, 500 nm/min; accumulation, 10; wavelengths, 400–190 nm). A detailed description of the experimental protocols and relevant parameters (retention times, stereochemical

purities) is provided in the Supporting Information.

2.1.1. General procedure of the synthesis of compounds 14–45

A mixture of pentagonal carbaldehyde **11a-d** (1 equiv.), alkyl acetoacetate **12a-b** (1 equiv.), guanidine derivative **13a-d** (1.5 equiv.) and Na₂CO₃ (1.5 equiv.) in DMF was stirred with orbital stirring at 70 °C for 15 hours. After completion of the reaction, as indicated by TLC, the solvent was removed in vacuum and the obtained oily residue was purified with flash chromatography at using Hex:AcOEt mixtures as mobile phase.

2.1.2. General procedure of the synthesis of compounds 46–61

A mixture of pentagonal carbaldehyde **11a-d** (1 equiv.), alkyl acetoacetate **12a-b** (1 equiv.), guanidine derivative **13e-f** (1.5 equiv.) in acetic acid was stirred with orbital stirring at 90 °C for 15 hours. After completion of the reaction, as indicated by TLC, the reaction mixture was diluted with 10 ml of water and carried to pH 8 with NaHCO₃, afterwards was extracted with AcOEt. The organic layer was dried with Na₂SO₄, filtered, and evaporated under vacuum. The obtained oily residue was purified with flash chromatography at using Hex:AcOEt mixtures as mobile phase.

2.1.3. General procedure of the synthesis of compounds 62–69

A mixture of pentagonal carbaldehyde **11a-d** (1.5 equiv.), alkyl acetoacetate **12a-b** (1.5 equiv.), 1-(1*H*-benzo[*d*]imidazol-2-yl)guanidine **13 g** (1 equiv.), catalyst-free, in THF was stirred in a sealed tube at 170 °C for 2 hours. After completion of the reaction, as indicated by TLC, the solvent was removed in vacuum and the obtained oily residue was purified with flash chromatography at using DCM:MeOH mixtures as mobile phase.

2.1.4. General procedure of the synthesis of compounds 70–125

A mixture of pentagonal carbaldehyde **11a-d** (1.5 equiv.), alkyl acetoacetate **12a-b** (1.5 equiv.), 1*H*-1,2,4-triazol-5-amine-3-substituted derivative **13 h-n** (1 equiv.), and zinc chloride (0.1 equiv.), in THF was stirred with orbital stirring at 90 °C for 12 hours. After completion of the reaction, as indicated by TLC, the solvent was removed in vacuum and the obtained oily residue was purified with flash chromatography at using Hex:AcOEt mixtures as mobile phase.

2.1.5. General procedure of the synthesis of compounds 126–133

A mixture of pentagonal carbaldehyde **11a-d** (1.5 equiv.), alkyl acetoacetate **12a-b** (1.5 equiv.), 1*H*-tetrazol-5-amine **13o** (1 equiv.), and *L*-proline (0.1 equiv.), in DMF was stirred with orbital stirring at 90 °C for 15 hours. After completion of the reaction, as indicated by TLC, the solvent was removed in vacuum and the obtained oily residue was purified with flash chromatography at using Hex:AcOEt mixtures as mobile phase.

2.1.6. General procedure of compounds 134–141 and 150–157

A mixture of pentagonal carbaldehyde **11a-d** (1equiv.), alkyl acetoacetate **12a-b** (1 equiv.), and 1,3-dinucleophile derivative [5-amino-1*H*-pyrazole-4-carbonitrile **13p** or thiazol-2-amine **13q**] (1.5 equiv.), and chloroacetic acid (0.1 equiv.), in DMF was stirred with orbital stirring at 90 °C for 15 hours. After completion of the reaction, as indicated by TLC, the solvent was removed in vacuum and the obtained oily residue was purified with flash chromatography at using Hex:AcOEt mixtures as mobile phase.

2.1.7. General procedure of the synthesis of compounds 142–149 and 158–181

A mixture of pentagonal carbaldehyde **11a-d** (1equiv.), alkyl acetoacetate **12a-b** (1 equiv.), and 1,3-dinucleophile derivative [1*H*-indazol-3-amine **13r**, benzo[*d*]thiazol-2-amine **13 s**, 5-chlorobenzo[*d*]thiazol-2-amine **13t**, or 6-chlorobenzo[*d*]thiazol-2-amine **13 u** (1.5 equiv.)] (1.5 equiv.), in acetic acid was stirred under microwave (Mw)

radiation at 90 °C for 9 hours. After completion of the reaction, as indicated by TLC, the reaction mixture was diluted with 10 ml of water and carried to pH 8 with NaHCO₃, afterwards was extracted with AcOEt. The organic layer was dried with Na₂SO₄, filtered, and evaporated under vacuum. The obtained oily residue was purified with flash chromatography at using DCM:MeOH mixtures as mobile phase.

2.2. Pharmacology

2.2.1. Pharmacology binding assays

Radioligand binding competition assays were performed *in vitro* using human ARs expressed in transfected HeLa [*hA*_{2A}AR (9 pmol/mg protein) and *hA*₃AR (3 pmol/mg protein)], HEK-293 [*hA*_{2B}AR (1.5 pmol/mg protein)] and CHO [*hA*₁AR (1.5 pmol/mg protein)] cells as described previously [16–21]. A brief description is given below. *A*₁AR competition binding experiments were carried out in membranes from CHO-*A*₁ cells labelled with 1 nM [³H]DPCPX (*K*_D = 0.7 nM). Non-specific binding was determined in the presence of 10 μM R-PIA. The reaction mixture was incubated at 25 °C for 60 min. *A*_{2A}AR competition binding experiments were carried out in membranes from HeLa-*A*_{2A} cells labelled with 3 nM [³H]ZM241385 (*K*_D = 2 nM). Non-specific binding was determined in the presence of 50 μM NECA. The reaction mixture was incubated at 25 °C for 30 min. *A*_{2B}AR competition binding experiments were carried out in membranes from HEK-293-*A*_{2B} cells (Euroscreen, Gosselies, Belgium) labelled with 25 nM [³H]DPCPX (*K*_D = 21 nM). Non-specific binding was determined in the presence of 400 μM NECA. The reaction mixture was incubated at 25 °C for 30 min. *A*₃AR competition binding experiments were carried out in membranes from HeLa-*A*₃ cells labelled with 10 nM [³H]NECA (*K*_D = 8.7 nM). Non-specific binding was determined in the presence of 100 μM R-PIA. The reaction mixture was incubated at 25 °C for 180 min. After the incubation time, membranes were washed and filtered, radioactivity was detected in a Microbeta Trilux reader (PerkinElmer).

2.2.2. Pharmacology functional experiments

The following reagents were used: adenosine deaminase (ADA, Roche Diagnostics, Mannheim, Germany), 5'-N-ethyl-carboxamido-adenosine (NECA, Tocris, Bristol, UK), zardaverine (Calbiochem, San Diego, California, USA). Human embryonic kidney (HEK)-293 T cells expressing the *hA*_{2B}AR (Reference 15) were grown in Dulbecco's modified Eagle's medium (DMEM) (Sigma-Aldrich, St. Louis, Missouri, USA) supplemented with 1 mM sodium pyruvate (Biowest, Nuaille, France), 2 mM L-glutamine (Biowest), 100 U/ml streptomycin (Biowest), 100 mg/ml penicillin (Biowest), and 5% (v/v) fetal bovine serum (Invitrogen, Carlsbad, California, USA) at 37°C and in an atmosphere of 5% CO₂.

2.2.3. cAMP accumulation assay

cAMP accumulation was measured using the LANCE Ultra cAMP kit (PerkinElmer, Waltham, MA, USA) as previously described [22]. In brief, HEK-293 T cells expressing the *hA*_{2B}AR were detached with accutase (Sigma-Aldrich) and incubated for 1 h at 22°C in Dulbecco's modified Eagle's medium (DMEM) (Sigma-Aldrich) supplemented with 0.1% BSA, ADA (0.5 U/ml) and zardaverine. *hA*_{2B}AR cells (500 cells/200 μl well) were incubated with NECA (300 nM) in the presence or absence of increasing concentrations of 47, 48, 63, 79, 87, 89, 111, 113, 159, 160, 161, 164, 168, 172, 176, and 177, during 30 min at 22°C. Eu-cAMP tracer and ULIGHT™-anti-cAMP reagents were prepared and added to the sample following manufacturer's instructions. The 384-wells plate was incubated 1 h at 22°C in the dark and was then read on a CLARIOstar microplate reader (BMG Labtech, Durham, NC, USA). Measurements at 665 nm and 620 nm were used to determine the TR-FRET signal ratio (665 nm/620 nm) and the concomitant cAMP levels were expressed as relative TR-FRET units (RFU = (1/TR-FRET ratio) x 10000). Data were fitted by non-linear regression using GraphPad Prism 10.0.2 (San Diego, CA, USA). Concentration-response

curves were carried out by assaying different 47, 48, 63, 79, 87, 89, 111, 113, 159, 160, 161, 164, 168, 172, 176, and 177 concentrations ranging between 10 nM to 30 μM. Data was expressed as *K*_B by following the formula reported by Leff and Dougall (Eq. (1)) [23].

$$K_B = \frac{IC_{50}}{(2 + ([A]/[A_{50}])^n)^{1/n}}$$

Equation 1. Correction offset value for all the ABFE estimates [23].

Where *IC*₅₀ is the concentration of compound that inhibits NECA effect by a 50%; [A] is the concentration of NECA employed in the assay, [A₅₀] is the NECA EC₅₀ value, and n is the Hill slope of the curve.

2.2.4. Data and statistical analysis

Data are represented as mean ± standard error of mean (SEM) with statistical significance set at P < 0.05. The number of samples (n) in each experimental condition is indicated in the corresponding figure legend. Outliers were assessed by the ROUT method [24], thus any sample was excluded assuming a Q value of 1% in GraphPad Prism 9 (San Diego, CA, USA). Comparisons among experimental groups were performed by Student's t test or one-way analysis of variance (ANOVA) followed by Tukey's multiple comparisons post-hoc test using GraphPad Prism 10.0.2, as indicated.

2.3. Computational

2.3.1. Receptor modeling and ligand docking

An homology model of the inactive form of the *hA*_{2B}AR was generated at the beginning of this project, and subsequently inserted into an atomistic model of the cellular membrane, followed by molecular dynamics (MD) equilibration under periodic boundary conditions (PBC) with the PyMemDyn protocol [25]. This model was subsequently refined along this project by antagonist docking, MD and FEP simulations [18], and herein prepared for docking of selected antagonists with the Protein Preparation Wizard pipeline in Maestro (Schrodinger ver. 2021–3) (coordinates provided as PDB file in Supplementary material). A receptor grid was generated with the default Van der Waals radius scaling settings, positioned in the centre of geometry of the binding site, and the size determined by the size of previously docked ligands from analogous series [18]. Ligand preparation involved generation of all 3D tautomers and protomers at pH 7 ± 2 with the same software, using the OPLS4 force field65 and Epik [26]. The lowest energy conformer for each molecular form was retained for receptor-ligand docking with Glide SP docking with default parameters [27].

2.3.2. FEP simulations

The membrane-equilibrated binding site used for docking was transferred to the MD software Q [28] for free energy perturbation (FEP) calculations under spherical boundary conditions. All preparations, MD simulations and analysis were managed with the automated QligFEP protocol [29], considering the following simulation parameters: A 25 Å sphere centered on the centre of geometry of the ligand was defined for unrestrained MD simulations, where only protein atoms in the boundary of the sphere (22–25 Å outer shell) had a positional restraint of 20 kcal/mol/Å². Solvent atoms were subject to polarization and radial restrains using the surface constrained all-atom solvent (SCAAS) [28,30] model to mimic the properties of bulk water at the sphere surface. Atoms lying outside the simulation sphere are tightly constrained (200 kcal/mol/Å² force constant) and excluded from the calculation of non-bonded interactions. Long range electrostatics interactions beyond a 10 Å cut off were treated with the local reaction field method [31], except for all ligand atoms, undergoing the FEP transformation, where no cut-off was applied. Solvent bond and angles were constrained using the SHAKE algorithm [32]. All titratable residues outside the sphere were neutralized and histidine residues were assigned a hydrogen atom on the δ nitrogen. Residue parameters were translated from the

OPLS-AA/M force field [33], ligand parameters generated with the FFLD server from Schrödinger, and POPC lipid Berger parameters were adopted [34]. The QligFEP protocol includes a warming-up equilibration phase of each complex consisting of 0.62 nanoseconds MD simulations, where temperature gradually rises from 1 to 298 K, while restraints of 10 kcal/mol/Å² initially imposed on all heavy atoms within the sphere are subsequently released. Thereafter each system is subject to a defined number of parallel replicates of unrestrained MD (in our case between 10 and 20), where the dual-topology QligFEP protocol is applied for each ligand transformation [29]. Each of these MD replicates starts with a 0.4 nanosecond unbiased equilibration period, with different initial velocities. The FEP protocol itself here adopted consists of 100 FEP λ -windows of 40 ps each, distributed using a sigmoidal function. The SHAKE algorithm was used to constraint bonds and angles. To fulfil a thermodynamic cycle and calculate relative binding free energies, parallel FEP transformations are run in a sphere of water for each ligand pair. In these water simulations, the same parameters apply (i.e., sphere size, simulation time, etc.), and the relative binding free energy difference between the ligand pair was estimated by solving the thermodynamic cycle utilizing the Bennett acceptance ratio (BAR) [35], reported as average values with the associated standard error of the mean (s.e.m.).

2.3.3. Quantum mechanical pK_a calculation

Isodesmic method or relative pK_a calculation [36] was used to calculate solution-phase pK_a values in water, following the formula: $pK_a = \frac{\Delta G_s}{RT} \ln(10) + pK_a(HREF)$, from the solution phase reaction free energy (ΔG_s) using the following proton transfer reaction: $HA + REF^- + HREF$, where HA and A⁻ represent examined acid and its conjugate base while REF and HREF represent reference base and its conjugate acid respectively. Reaction free energy is calculated as the difference between free energies of products and reactants according to the formula: $\Delta G_s = (G(A^-) + G(REF^-)) - (G(HA) + G(HREF))$. The reference base should be as chemically similar as possible to the group whose pK_a is to be determined, in this case the thiol group on the aromatic ring, thus thiophenol was selected as referent base [37–39].

As a good compromise between accuracy and feasibility, all geometries optimizations and free energy calculations were carried out by the very efficient M06–2X/6–31+G(d) method. SMD continuum model [40] was considered to account solvent effects during both geometry optimization and energy calculation, with parameters corresponding to pure water. All calculations were performed using the Gaussian 16 software [41].

2.4. Antiproliferative assays

2.4.1. Cell culture

HCT116 cell lines were purchased from the American Type Culture Collection (ATCC) and cultured in DMEM GlutaMAX (ThermoFisher Scientific), supplemented with 10% Fetal Bovine Serum (FBS) (ThermoFisher Scientific) and 1% Penicillin Streptomycin (PS). GlutaMAX supplement (2 mM) was added for HCT116 culture. Cell cultures were regularly tested for the presence of mycoplasma. Human colorectal Cancer Associated Fibroblasts (CAFs) primary cultures were obtained and immortalized as described in bibliography [42,43], and maintained in DMEM GlutaMAX, 10% FBS, 1% Insulin Transferrin Selenium (ITS) (ThermoFisher Scientific).

2.4.2. Proliferation assays

To test the effect of A_{2B}AR (and dual A_{2A}AR/A_{2B}AR) antagonism on the proliferation, different cell lines were seeded on a 96-well in complete medium (5000 cells/well for HCT-116 and CAFs, 20,000 cells/well for primary cell line) and incubated overnight to allow attachment. Cells were then incubated for 24 h or 48 h with solutions containing **159**, **164** or **176** at 2.5, 5 and 10 μ M in complete medium. For three-dose assays,

cells were incubated for 72 hours with a dose applied every 24 hours. Controls with the equivalent amount of DMSO, used as the solvent for the indicated antagonists, were as well performed. After incubation, the number of viable cells was determined by using AlamarBlue (10%, ThermoFisher Scientific) following manufacturer's recommendations, measuring fluorescence at 590 nm. Proliferation rates for each condition were represented as % proliferation respect to the appropriate DMSO controls.

2.4.3. ADORA gene expression analysis

To assess the gene expression of ADORA2A and ADORA2B genes, RNA was first extracted from cell cultures of HCT116 and CAFs cell lines using the RNAeasy Mini kit (Qiagen), following manufacturer's protocol. After RNA quantification (Nanodrop, ThermoFisher Scientific), cDNA was synthesized using the M-muLV reverse transcriptase kit (Roche) as indicated by the manufacturer and used for downstream gene expression analysis using the following TaqMan probes (ThermoFisher Scientific): human ADORA2A (Hs00169123_m1) human ADORA2B (Hs00386497_m1) mouse Adora2A (Mm00802075_m1) mouse Adora2B (Mm00839292_m1). The expression of GAPDH was used as a control to normalize results across samples (human GAPDH: Hs999999905_m1; mouse Gapdh: Mm99999915_g1). 60 ng of total cDNA were loaded per well, and qPCR was run following standard recommended conditions on a QuantStudio 3 qPCR system (Applied Biosystems). GPCR expression was calculated as *Absolute gene expression* = $40 - \Delta Cq$. ΔCq values were calculated by subtracting raw Cq values for each cancer cell line to the Cq value obtained for GAPDH. The final obtained values were then transformed to a Log₂ scale for visualization purposes, calculating the fold change between two different cell lines with *Fold change* = $2^{-\Delta\Delta Cq}$, with $\Delta\Delta Cq$ being the difference of two different genes ΔCq .

2.4.4. Confocal imaging

Images were acquired on an inverted confocal microscope (Leica SP8) using laser lanes 405, 488, 561 and 533 nm, an HC-PL-APO CS2 40x/1.30 oil immersion objective, and non-descanned HyD detectors. For each experiment and stage position a Zstack was acquired with a Zstep of 1 μ m. For data visualization, a representative Z position was selected for each image stack.

2.4.5. EdU incorporation assays and cleaved Caspase 3 immunostaining

After the specified treatment times, cancer cells/CAFs were incubated for 30 min with a 10 μ M EdU solution in a complete medium. Cells were then fixed, and EdU incorporation was revealed as recommended, using the Click-iT EdU Alexa Fluor 647 Imaging kit (ThermoFisher Scientific). The same sample was then used to assess apoptosis using cleaved caspase 3 as a marker. For this, samples were blocked with 3% BSA (w/v) in PBS (v/v) solution for 1 h at RT. Primary antibody were prepared in a 0.05% Tx100/PBS (v/v) solution and incubated overnight in humidified chambers at RT. Cells were then washed 3 times with PBS and incubated with secondary antibodies and DAPI, for 1 h at RT, washed 3 times in PBS and mounted using AquaPolyMount (Polysciences). Antibodies references and dilutions are listed in [Supplementary Table S1](#).

2.4.6. Image analysis

For EdU and Cleave Caspase 3 staining's, 10–15 random images were taken per condition. The total number of cells was determined based on the DAPI channel and quantified automatically using an Image J (Fiji) v2.3.0/1.53 f homemade macro. The total number of cells positive for EdU and Cleaved Caspase 3 was quantified manually and plotted as % to the total number of cells per analysed field.

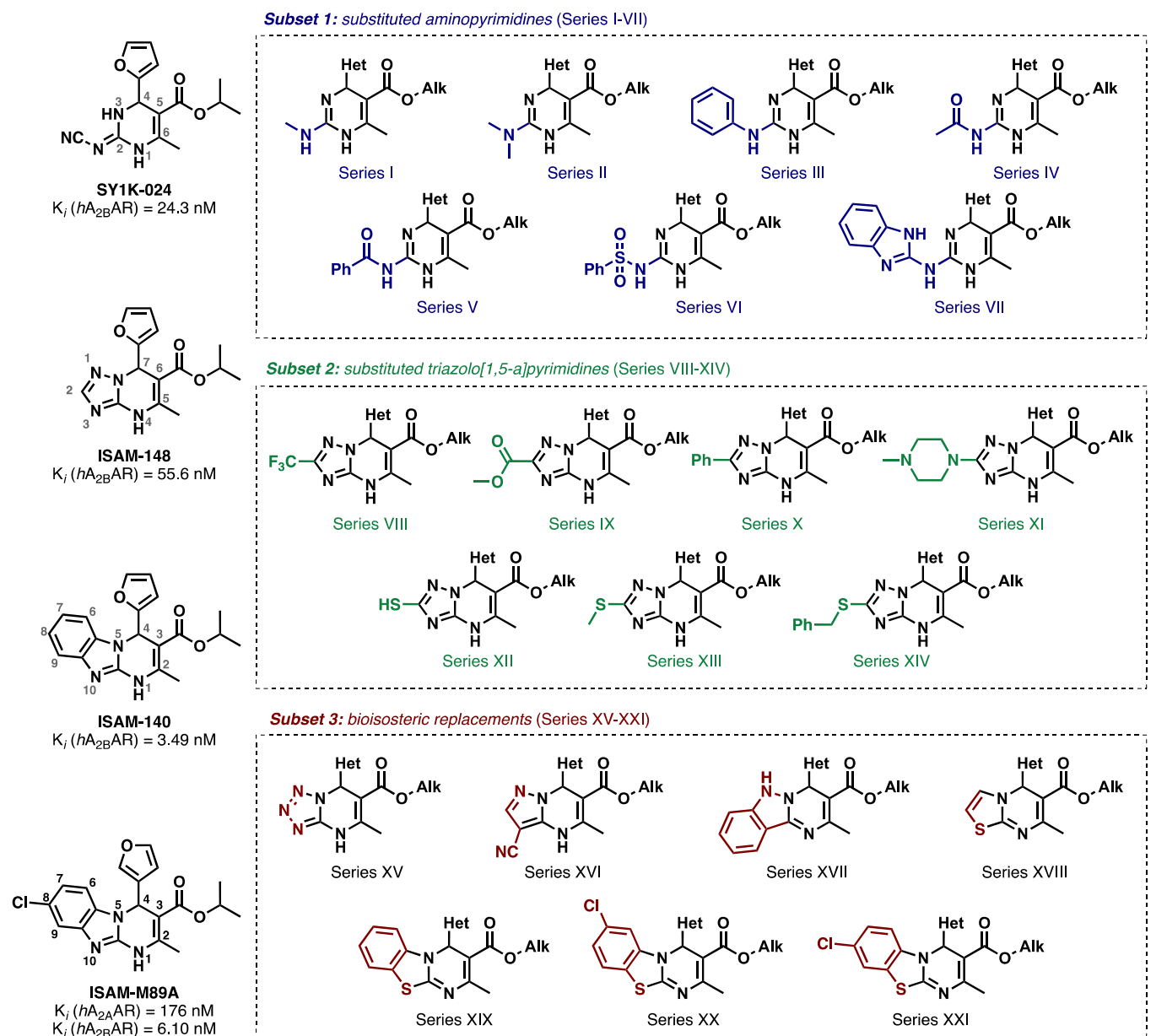


Fig. 2. Strategy for the design of novel $A_{2B}AR$ antagonists from mono-, bi-, and tricyclic cores from model series I-III. In blue (top), 2-substituted monocycles series (Subset 1). In green (middle), 2-substitutions bicycles series (Subset 2). In magenta (bottom), bioisosteric replacements series (Subset 3). Het = Heteroaryl (2-furyl, 3-furyl, 2-thienyl or 3-thienyl), Alk = Alkyl (ethyl or isopropyl).

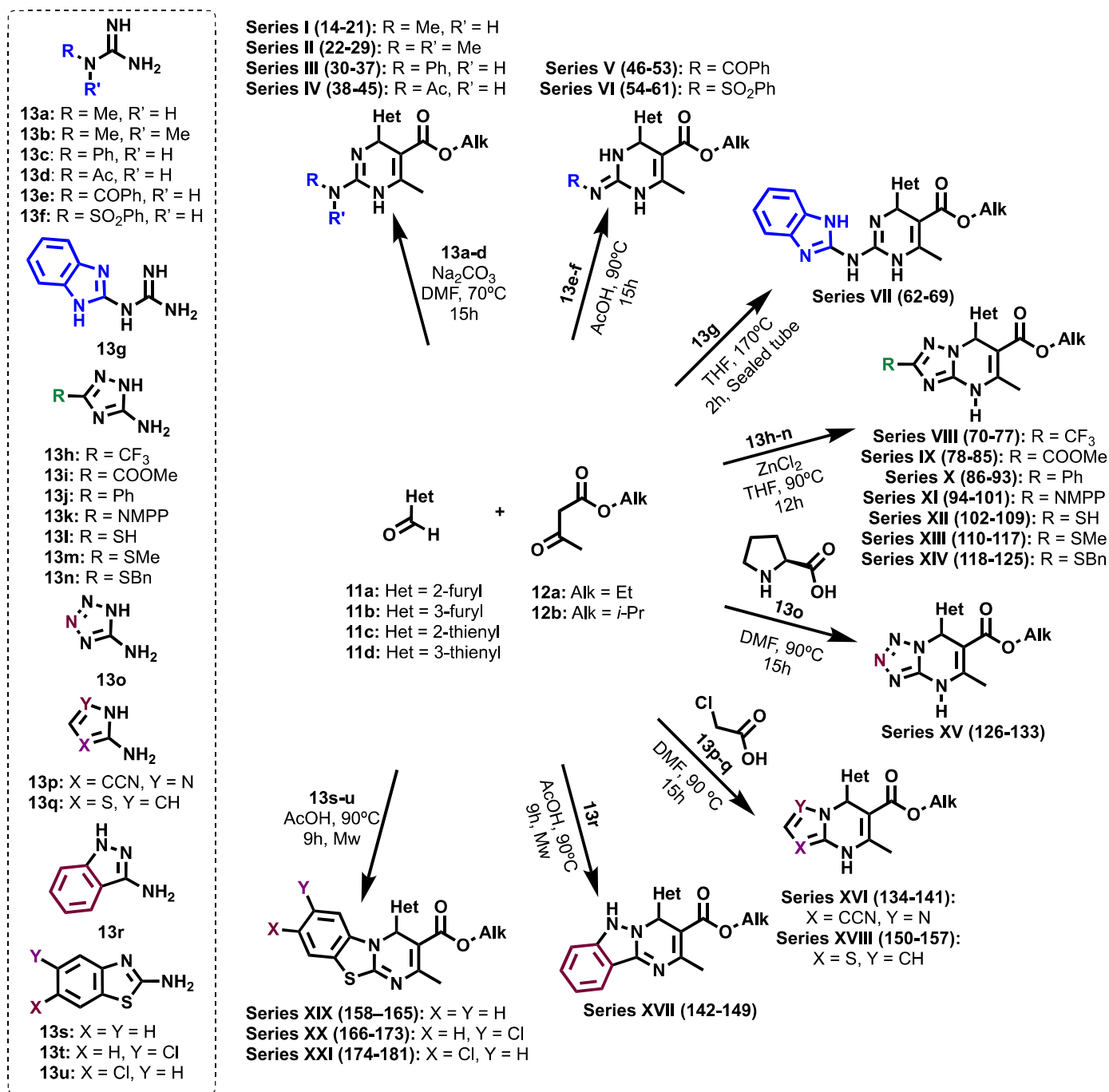
3. Results and discussion

3.1. Design

The starting point for this project was the previously reported monocyclic, bicyclic, and tricyclic pyrimidine derivatives (Fig. 1, compounds 7-10), which emerged from ongoing optimization projects aimed at developing selective $A_{2B}AR$ antagonists. Following a structure-based design program, we originally defined the binding mode of these scaffolds using a homology-based model of the $A_{2B}AR$ [16-18], and used it as a guide to explore different points of variability around the scaffold: optimal diversity for aldehyde and ester precursors, better positions of fusion [17], the impact of bioisosteric replacements for the pentagonal ring [19], and the introduction of halogens into aromatic [18] and aliphatic [20] scaffold positions. The SAR data from these studies strengthened and refined our structural model of stereoselective binding

to the $A_{2B}AR$. An integrative approach, leveraging the Biginelli reaction exploratory capabilities and our SAR observations, laid the foundation for designing 168 new pyrimidine derivatives. These series were subsequently synthesized and characterized at both the pharmacological and structural levels. The entire collection of compounds was divided into twenty-one series (series I-XXI), according to the design scheme depicted in Fig. 2.

This study showcased a systematic exploration of scaffolds through Biginelli chemistry, expanding the diversity within the pharmacophore space. In some cases, the assessment of heterocyclic cores extended beyond the substitution patterns recommended by the models (e.g., series XVII-XXI). The novelty of these series lies in their exploration of innovative substitution patterns on mono-, bi-, and tricyclic pyrimidine-based cores, while preserving optimal groups $A_{2B}AR$ affinity. These unaltered elements are present at the ester group, featuring ethyl or isopropyl alkoxy residues, as well as within the pentagonal cores,



Scheme 1. Biginelli-based synthesis of novel mono-, bi-, and tricyclic pyrimidinone derivatives.

featuring heteroaryl groups like 2-furyl, 3-furyl, 2-thienyl, and 3-thienyl. Consequently, each of the twenty-one series described below is composed by the eight possible combinations (Tables 1–9), and is further divided into three subsets (Fig. 2).

The first subset, series I–VII (Tables 1–4), comprises monocyclic compounds (2-aminopyrimidines) that explore diverse substituents at position 2 (Fig. 2). The design of these series combined the exploration of different exocyclic amino groups' impact in monocyclic scaffolds [16, 21], (series I, II and III composed by methylamino-, dimethylamino-, and phenylamino- pyrimidines respectively, compounds 14–37, Table 2) and includes ring-opening strategies from bicyclic derivatives [17] (series IV, V and VI constituted by 2-acetamido-, 2-benzamido-, and 2-phenylsulphonamido pyrimidine derivatives, compounds 38–61, Tables 2 and 3). The design of series VII (compounds 62–69, Table 4) is

based on the ring opening strategy of tricyclic compounds (Fig. 2), with the potential establishment of an intramolecular hydrogen bond according to our reported binding mode [17]. Another difference among these series is the prevalence of different major tautomer populations, which will come into play when establishing their SAR (see below).

The second subset, series VIII–XIV (Tables 5 and 6), systematic explores the position 2 of the bicyclic scaffold present in ISAM-148 (Fig. 1, compound 8a), combined with the selected Het and Alk substituents shown above. In Table 5, series VIII, IX, X, and XI explore carbon-based residues, including trifluoromethyl, methoxycarbonyl, and phenyl, as well as 4-methylpiperazin-1-yl. Table 6, on the other hand, showcases series XII, XIII, and XIV, which delve into sulphur-based groups, namely thiol, methylthio, and benzylthio residues.

The final subset, series XV–XXI, is based on various design strategies

around bi- and tricyclic compounds (Fig. 2). Series XV explores the classical CH/N bioisosterism at position 2 of the model bicyclic scaffold (ISAM-148, Fig. 2), obtaining tetrazole derivatives. Series XVI explores the exocyclization of the imine-type nitrogen at position 3 of ISAM-148, introducing a cyano group. On the other hand, series XVII was conceived with the disconnection and reconnection of the central heterocycle within the tricyclic derivative ISAM-140 (see Fig. 2). The last four series within this group (XVIII–XXI, compounds 158–181) were designed to explore the actual consequences of eliminating the characteristic double hydrogen bond of the pattern series at the orthosteric site of the A_{2B}AR. They involve N/S replacements in the pentagonal core of ISAM-140 and ISAM-148, thus generating alternative binding modes. Specifically, series XVIII and XIX replace the imidazole with a thiazole ring, lacking the NH hydrogen bond donor group. Finally, a focused series consisting of benzo[4,5]thiazolo[3,2-*a*]pyrimidines with a chlorine atom at positions 7 (series XX) or 8 (series XXI), which we recently identified as optimal halogenated patterns for tricyclic derivatives (Fig. 1, compounds 9c and 10) [18], was obtained to further explore the interaction with the deeper binding pocket of the A_{2B}AR as well as the dual A_{2A}AR/A_{2B}AR behaviour.

3.1.1. Chemistry

All the compounds (14–181) were synthesized as outlined in Scheme 1. A three-component synthesis, based on the robust and efficient Biginelli reaction (i.e., the three-component reaction of an aldehyde, a β -ketoester and 1,3-dinucleophiles), allowed for a time- and cost-effective assembly of the large collection obtained. A set of pentagonal carbaldehydes (11a–d) and β -ketoesters (12a–b) providing optimal substituents for positions 4 and 3 in combination with different 1,3-dinucleophiles (13a–u) were used as precursors. The reaction conditions, highly dependent on the nature of the 1,3-dinucleophile, vary for the different series, with seven experimental conditions for the synthesis of all the series (Scheme 1).

A detailed description of the synthetic procedures is available in the Supporting Information. Briefly, the precursors, dissolved in THF, DMF, acetic acid, or their mixtures, and containing a catalytic amount of Na₂CO₃, ZnCl₂, acetic acid, or chloroacetic acid (Scheme 1), were subjected to orbital stirring at 70–90 °C, 90 °C under microwave irradiation or 170 °C in a sealed tube; from 2 to 16 h, affording satisfactory yields for all the series. All reactions were monitored by thin-layer chromatography (TLC). Upon reaction completion, the solvent was evaporated off, and the isolated solid was purified using column chromatography on silica gel. A detailed description of the synthetic methods and the complete structural, spectroscopic, and analytical data for all compounds are provided in the Experimental Section. As in previous series (Fig. 1, compounds 7–10) all ligands obtained in this study contain one stereocenter at the pyrimidine core (heteroaryl; Het) and they were isolated and evaluated as racemic mixtures. Two compounds eliciting attractive A_{2B}AR affinity/selectivity profile and one dual A_{2A}AR/A_{2B}AR ligand were submitted to chiral resolution to isolate their corresponding enantiomer pairs. The configuration of these enantiomers was unequivocally determined using circular dichroism (CD), following methodologies described in prior works [18].

3.2. Biological evaluation

The adenosinergic profile (affinity and selectivity) of the 168 novel compounds was evaluated *in vitro* using radioligand binding assays at the four human AR subtypes [16,17,20,21]. Table 1 encompasses the binding data from model series I–III. Tables 2–8 contain the binding data obtained for the new compounds. All reported ligands were obtained and tested as racemic mixtures. The entire set was evaluated *in silico* using the PAINS filter in RDkit [44] to rule out the possibility that these ligands being promiscuous pan-assay interference compounds (PAINS). Human ARs were expressed in transfected cell lines [e.g., Chinese hamster ovary (CHO) cells (A₁AR), human epithelial carcinoma (HeLa)

cells (A_{2A}AR and A₃AR) and human embryonic kidney (HEK-293) cells (A_{2B}AR)]. [³H]DPCPX for A₁AR and A_{2B}AR, [³H]NECA for A₃AR, and [³H]ZM241385 for A_{2A}AR were used as radioligands. The binding data is presented as K_i ± SEM (nM, n = 3) or as specific binding inhibition percentage at 1 μ M (n = 2, average) for compounds that did not completely displace the radioligand. K_i values were acquired by fitting the data by nonlinear regression using Prism 5.0 software (GraphPad, San Diego, CA). A specific percentage binding inhibition is reported for those compounds that exhibited low affinity. The results are the average of three experiments, each of which was performed in duplicate. A set of well-known AR ligands (ISAM-140, DPCPX, NECA and ZM241385) was assessed using our experimental protocols; their binding data are reported in tables. The stereoisomers obtained by chiral resolution were tested in all four human AR subtypes in their enantiopure forms (Table 9). This data were used to complement the SAR study and to evaluate the importance of the stereogenic centre configuration on the affinity in the novel series.

3.3. Intrinsic activity assays

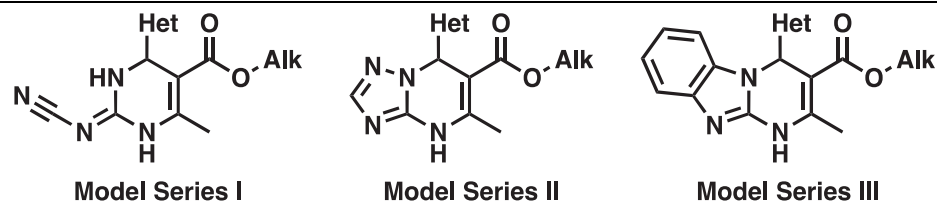
Sixteen representative derivatives (47, 48, 63, 79, 87, 89, 111, 113, 159, 160, 161, 164, 168, 172, 176, and 177) were selected to obtain information on the functional effect of the different series of A_{2B}AR ligands obtained. Thus, we assessed their ability to block the intrinsic activity of the non-selective A_{2B}AR agonist NECA. To this end, the effect on agonist-induced A_{2B}AR-mediated cAMP accumulation in HEK293 cells expressing the receptor was evaluated, as previously described [18]. NECA triggered concentration-dependent cAMP accumulation in A_{2B}AR cells with an EC₅₀ of 169 nM (95% CI: 134 – 212 nM) (Fig. 3A). Hence, A_{2B}AR cells were challenged with NECA (300 nM) in the absence or presence of increasing concentrations of 47, 48, 63, 79, 87, 89, 111, 113, 159, 160, 161, 164, 168, 172, 176, and 177 and the K_B value for each compound was calculated (Fig. 3B). Three molecules, 160, 176 and 177 showed K_B values below 100 nM (i.e., 36 nM, 37 nM, and 87 nM, respectively) (Fig. 3B).

A set of five molecules displayed moderate K_B values, ranging between 100 nM and 200 nM (i.e., 159, 161, 89, 87, and 164), while the remaining derivatives (i.e., 63, 168, 113, 172, 47, 111, 79, and 48) elicited K_B values between 200 nM and 1 μ M (Fig. 3B). In general, all the molecules tested displayed high to moderate potency blocking A_{2B}AR-mediated cAMP accumulation, thus unequivocally indicating an antagonist intrinsic activity nature.

3.4. Structure-activity relationship studies and molecular modeling

This section describes the structure affinity (SAR) and structure-selectivity (SSR) relationships arising from the pharmacological data obtained for the whole series (Tables 2–8). The establishment of the SAR was driven by our computational modeling of adenosine receptors and the interaction with their ligands, which involves a combination of homology modeling of the hA_{2B}AR, ligand-receptor docking and free energy calculations, as recently reviewed [45], here also including quantum calculations. Comparing our MD-equilibrated homology-based model of the hA_{2B}AR's inactive state with the recently reported cryo-EM structure of its active, G protein-bound state [46] reveals a strong correlation of the orientation of the side chains within the orthosteric binding site (RMSD = 1.87, considering all main and side chains' heavy atoms within 5 Å of compound 176 docked as a reference, after superimposing both structures based on their C α trace). Following standard GPCR-ligand design procedures, we preferred our computer-generated model of the receptor's inactive form for antagonist design, as the active state presents the typical conformational changes of the helices involved in receptor activation. Where relevant, we compare the new data with the affinities and established SAR of the three series of model [monocyclic, bicyclic, and tricyclic] derivatives (Table 1). All the pharmacological data presented along this section corresponds to the

Table 1
Structure and adenosine receptor binding affinities of model series I-III [17,21].



Comp.	Het	Alk	K_i (nM) or % at 1 μ M			
			$hA_1^{a,b}$	$hA_{2A}^{b)}$	$hA_{2B}^{c)}$	$hA_3^{d)}$
Ia	2-furyl	Et	27%	20%	900 \pm 6	20%
Ib (SY1K-024)	2-furyl	i-Pr	21%	19%	24.3 \pm 0.9	4%
Ic	3-furyl	Et	28%	31%	102 \pm 3	14%
Id	3-furyl	i-Pr	34%	25%	59.4 \pm 1.8	41%
Ie	2-thienyl	Et	26%	33%	51.0 \pm 2.1	3%
If	2-thienyl	i-Pr	31%	16%	349 \pm 3	27%
Ig	3-thienyl	Et	29%	30%	461 \pm 2	23%
Ih	3-thienyl	i-Pr	11%	18%	657 \pm 4	13%
IIa	2-furyl	Et	15%	20%	3%	4%
IIb (ISAM-148)	2-furyl	i-Pr	2%	5%	55.6 \pm 4	2%
IIc	3-furyl	Et	2%	1%	602 \pm 10	4%
IId	3-furyl	i-Pr	2%	2%	350 \pm 8	20%
IIE	2-thienyl	Et	1%	2%	15%	15%
IIf	2-thienyl	i-Pr	1%	1%	1%	3%
IIg	3-thienyl	Et	3%	21%	699 \pm 5	2%
IIh	3-thienyl	i-Pr	3%	2%	816 \pm 7	5%
IIIa (ISAM-134)	2-furyl	Et	5%	14%	12.0 \pm 0.7	1%
IIIb (ISAM-140)	2-furyl	i-Pr	20%	25%	3.49 \pm 0.2	2%
IIIc (ISAM-141)	3-furyl	Et	7%	11%	20.6 \pm 1.1	1%
IIId (ISAM-142)	3-furyl	i-Pr	12%	22%	11.40 \pm 0.5	2%
IIIe	2-thienyl	Et	8%	16%	484 \pm 3	1%
IIIf	2-thienyl	i-Pr	1%	17%	371 \pm 5	3%
IIIg	3-thienyl	Et	3%	10%	29.7 \pm 1.2	2%
IIIh	3-thienyl	i-Pr	11%	3%	29.3 \pm 1.1	21%
ISAM-140	-	-	20%	25%	3.49 \pm 0.2	20%
DPCPX	-	-	2.20 \pm 0.2	157 \pm 3	73.24 \pm 1.4	1722 \pm 11
ZM241385	-	-	683 \pm 4	1.9 \pm 0.1	65.7 \pm 1.1	863 \pm 4
NECA	-	-	14.0 \pm 1	20.0 \pm 3	2400 \pm 35	6.20 \pm 9

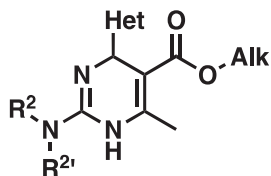
^a Displacement of specific [³H]DPCPX binding in human CHO cells expressed as K_i in nM (n = 3) or percentage displacement of specific binding at a concentration of 1 μ M (n = 2).

^b Displacement of specific [³H]4-(2-[7-amino-2-(2-furyl)[1,2,4]triazolo[2,3-a][1,3,5]triazin-5-ylamino]ethyl)phenol binding in human HeLa cells expressed as K_i in nM (n = 3) or percentage displacement of specific binding at a concentration of 1 μ M (n = 2).

^c Displacement of specific [³H]DPCPX binding in human HEK-293 cells expressed as K_i in nM (n = 3) or percentage displacement of specific binding at a concentration of 1 μ M (n = 2).

^d Displacement of specific [³H]NECA binding in human HeLa cells expressed as K_i in nM (n = 3) or percentage displacement of specific binding at a concentration of 1 μ M (n = 2).

Table 2
Structure and adenosine receptor binding affinities of series I-III.



Series I: Compounds 14-21

Series II: Compounds 22-29

Series III: Compounds 30-37

Comp.	R ²	R ^{2'}	Het	Alk	K _i (nM) or % at 1 μM			
					hA ₁ ^{a)}	hA _{2A} ^{b)}	hA _{2B} ^{c)}	hA ₃ ^{d)}
14	Me	H	2-furyl	Et	4%	8%	26%	2%
15	Me	H	2-furyl	<i>i</i> -Pr	18%	3%	21%	10%
16	Me	H	3-furyl	Et	22%	15%	33%	22%
17	Me	H	3-furyl	<i>i</i> -Pr	4%	6%	20%	18%
18	Me	H	2-thienyl	Et	27%	2%	7%	25%
19	Me	H	2-thienyl	<i>i</i> -Pr	10%	7%	20%	13%
20	Me	H	3-thienyl	Et	16%	16%	16%	21%
21	Me	H	3-thienyl	<i>i</i> -Pr	2%	12%	53%	7%
22	Me	Me	2-furyl	Et	16%	45%	19%	3%
23	Me	Me	2-furyl	<i>i</i> -Pr	15%	1%	1%	13%
24	Me	Me	3-furyl	Et	3%	9%	20%	11%
25	Me	Me	3-furyl	<i>i</i> -Pr	4%	17%	11%	5%
26	Me	Me	2-thienyl	Et	29%	27%	3%	15%
27	Me	Me	2-thienyl	<i>i</i> -Pr	8%	21%	1%	3%
28	Me	Me	3-thienyl	Et	11%	13%	8%	12%
29	Me	Me	3-thienyl	<i>i</i> -Pr	22%	12%	10%	5%
30	Ph	H	2-furyl	Et	13%	3%	13%	15%
31	Ph	H	2-furyl	<i>i</i> -Pr	18%	8%	56%	27%
32	Ph	H	3-furyl	Et	4%	20%	15%	18%
33	Ph	H	3-furyl	<i>i</i> -Pr	15%	17%	34%	5%
34	Ph	H	2-thienyl	Et	21%	6%	41%	20%
35	Ph	H	2-thienyl	<i>i</i> -Pr	9%	12%	1%	11%
36	Ph	H	3-thienyl	Et	23%	22%	28%	24%
37	Ph	H	3-thienyl	<i>i</i> -Pr	1%	9%	37%	17%
ISAM-140	-	-	-	-	20%	25%	3.49 ± 0.2	20%
DPCPX	-	-	-	-	2.20 ± 0.2	157 ± 3	73.24 ± 1.4	1722 ± 11
ZM241385	-	-	-	-	683 ± 4	1.9 ± 0.1	65.7 ± 1.1	863 ± 4
NECA	-	-	-	-	14.0 ± 1	20.0 ± 3	2400 ± 35	6.20 ± 9

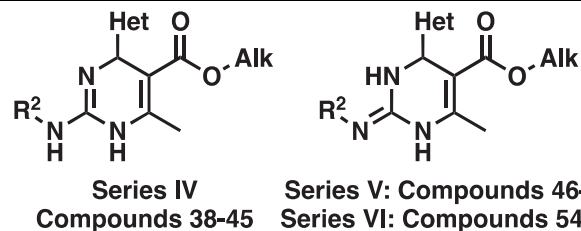
^a Displacement of specific [³H]DPCPX binding in human CHO cells expressed as K_i in nM (n = 3) or percentage displacement of specific binding at a concentration of 1 μM (n = 2).

^b Displacement of specific [³H]4-(2-[7-amino-2-(2-furyl)[1,2,4]triazolo[2,3-a][1,3,5]triazin-5-ylamino]ethyl)phenol binding in human HeLa cells expressed as K_i in nM (n = 3) or percentage displacement of specific binding at a concentration of 1 μM (n = 2).

^c Displacement of specific [³H]DPCPX binding in human HEK-293 cells expressed as K_i in nM (n = 3) or percentage displacement of specific binding at a concentration of 1 μM (n = 2).

^d Displacement of specific [³H]NECA binding in human HeLa cells expressed as K_i in nM (n = 3) or percentage displacement of specific binding at a concentration of 1 μM (n = 2).

Table 3
Structure and adenosine receptor binding affinities of series IV-VI.



Comp.	R ²	Het	Alk	K _i (nM) or % at 1 μM			
				hA ₁ ^{a)}	hA _{2A} ^{b)}	hA _{2B} ^{c)}	hA ₃ ^{d)}
38	COMe	2-furyl	Et	4%	9%	3%	1%
39	COMe	2-furyl	<i>i</i> -Pr	12%	5%	35%	14%
40	COMe	3-furyl	Et	3%	11%	15%	6%
41	COMe	3-furyl	<i>i</i> -Pr	7%	3%	31%	3%
42	COMe	2-thienyl	Et	3%	6%	3%	14%
43	COMe	2-thienyl	<i>i</i> -Pr	1%	4%	2%	4%
44	COMe	3-thienyl	Et	15%	6%	1%	7%
45	COMe	3-thienyl	<i>i</i> -Pr	6%	3%	8%	21%
46	COPh	2-furyl	Et	13%	17%	126 ± 2	9%
47	COPh	2-furyl	<i>i</i> -Pr	5%	8%	83.5 ± 0.8	4%
48	COPh	3-furyl	Et	2%	6%	148 ± 1.1	11%
49	COPh	3-furyl	<i>i</i> -Pr	3%	2%	227 ± 2.2	7%
50	COPh	2-thienyl	Et	4%	12%	3%	4%
51	COPh	2-thienyl	<i>i</i> -Pr	11%	5%	18%	8%
52	COPh	3-thienyl	Et	4%	3%	39%	16%
53	COPh	3-thienyl	<i>i</i> -Pr	5%	9%	50%	31%
54	SO ₂ Ph	2-furyl	Et	7%	1%	459 ± 4	5%
55	SO ₂ Ph	2-furyl	<i>i</i> -Pr	2%	4%	375 ± 3	21%
56	SO ₂ Ph	3-furyl	Et	6%	5%	15%	10%
57	SO ₂ Ph	3-furyl	<i>i</i> -Pr	1%	4%	25%	2%
58	SO ₂ Ph	2-thienyl	Et	2%	3%	7%	4%
59	SO ₂ Ph	2-thienyl	<i>i</i> -Pr	4%	1%	7%	3%
60	SO ₂ Ph	3-thienyl	Et	5%	2%	11%	15%
61	SO ₂ Ph	3-thienyl	<i>i</i> -Pr	3%	7%	16%	4%
ISAM-140	-	-	-	20%	25%	3.49 ± 0.2	20%
DPCPX	-	-	-	2.20 ± 0.2	157 ± 3	73.24 ± 1.4	1722 ± 11
ZM241385	-	-	-	683 ± 4	1.9 ± 0.1	65.7 ± 1.1	863 ± 4
NECA	-	-	-	14.0 ± 1	20.0 ± 3	2400 ± 35	6.20 ± 9

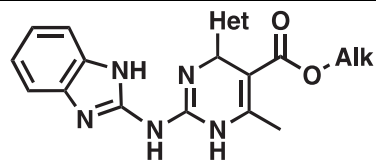
^a Displacement of specific [³H]DPCPX binding in human CHO cells expressed as K_i in nM (n = 3) or percentage displacement of specific binding at a concentration of 1 μM (n = 2).

^b Displacement of specific [³H]4-(2-[7-amino-2-(2-furyl)[1,2,4]triazolo[2,3-*a*][1,3,5]triazin-5-ylamino]ethyl)phenol binding in human HeLa cells expressed as K_i in nM (n = 3) or percentage displacement of specific binding at a concentration of 1 μM (n = 2).

^c Displacement of specific [³H]DPCPX binding in human HEK-293 cells expressed as K_i in nM (n = 3) or percentage displacement of specific binding at a concentration of 1 μM (n = 2).

^d Displacement of specific [³H]NECA binding in human HeLa cells expressed as K_i in nM (n = 3) or percentage displacement of specific binding at a concentration of 1 μM (n = 2).

Table 4
Structure and adenosine receptor binding affinities of series VII.



Series VII: Compounds 62-69

Comp.	Het	Alk	K_i (nM) or % at 1 μ M			
			$hA_1^{a)}$	$hA_{2A}^{b)}$	$hA_{2B}^{c)}$	$hA_3^{d)}$
62	2-furyl	Et	23%	13%	429 \pm 2	26%
63	2-furyl	<i>i</i> -Pr	13%	8%	127 \pm 1.3	21%
64	3-furyl	Et	3%	3%	40%	15%
65	3-furyl	<i>i</i> -Pr	28%	12%	480 \pm 4	23%
66	2-thienyl	Et	23%	9%	32%	42%
67	2-thienyl	<i>i</i> -Pr	6%	6%	11%	13%
68	3-thienyl	Et	18%	10%	34%	7%
69	3-thienyl	<i>i</i> -Pr	11%	6%	45%	17%
ISAM-140	-	-	20%	25%	3.49 \pm 0.2	20%
DPCPX	-	-	2.20 \pm 0.2	157 \pm 3	73.24 \pm 1.4	1722 \pm 11
ZM241385	-	-	683 \pm 4	1.9 \pm 0.1	65.7 \pm 1.1	863 \pm 4
NECA	-	-	14.0 \pm 1	20.0 \pm 3	2400 \pm 35	6.20 \pm 9

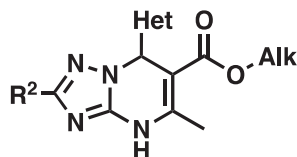
^a Displacement of specific [³H]DPCPX binding in human CHO cells expressed as K_i in nM (n = 3) or percentage displacement of specific binding at a concentration of 1 μ M (n = 2).

^b Displacement of specific [³H]4-(2-[7-amino-2-(2-furyl)[1,2,4]triazolo[2,3-a][1,3,5]triazin-5-ylamino]ethyl)phenol binding in human HeLa cells expressed as K_i in nM (n = 3) or percentage displacement of specific binding at a concentration of 1 μ M (n = 2).

^c Displacement of specific [³H]DPCPX binding in human HEK-293 cells expressed as K_i in nM (n = 3) or percentage displacement of specific binding at a concentration of 1 μ M (n = 2).

^d Displacement of specific [³H]NECA binding in human HeLa cells expressed as K_i in nM (n = 3) or percentage displacement of specific binding at a concentration of 1 μ M (n = 2).

Table 5
Structure and adenosine receptor binding affinities of series VIII-XI.



Series VIII: Compounds 70-77 **Series X: Compounds 86-93**
Series IX: Compounds 78-85 **Series XI: Compounds 94-101**

Comp.	R ²	Het	Alk	K _i (nM) or % at 1 μM			
				hA ₁ ^(a)	hA _{2A} ^(b)	hA _{2B} ^(c)	hA ₃ ^(d)
70	CF ₃	2-furyl	Et	22%	7%	839 ± 4	2%
71	CF ₃	2-furyl	<i>i</i> -Pr	30%	14%	589 ± 3	1%
72	CF ₃	3-furyl	Et	20%	25%	1219 ± 8	1%
73	CF ₃	3-furyl	<i>i</i> -Pr	8%	23%	1032 ± 5	1%
74	CF ₃	2-thienyl	Et	18%	17%	1%	3%
75	CF ₃	2-thienyl	<i>i</i> -Pr	16%	1%	54%	1%
76	CF ₃	3-thienyl	Et	1%	1%	840 ± 3.2	16%
77	CF ₃	3-thienyl	<i>i</i> -Pr	1%	2%	52%	7%
78	COOMe	2-furyl	Et	27%	36%	429 ± 2	2%
79	COOMe	2-furyl	<i>i</i> -Pr	7%	1%	41.4 ± 0.8	2%
80	COOMe	3-furyl	Et	4%	8%	22%	3%
81	COOMe	3-furyl	<i>i</i> -Pr	2%	19%	126 ± 2.2	11%
82	COOMe	2-thienyl	Et	8%	5%	6%	1%
83	COOMe	2-thienyl	<i>i</i> -Pr	17%	3%	1%	4%
84	COOMe	3-thienyl	Et	18%	10%	5%	1%
85	COOMe	3-thienyl	<i>i</i> -Pr	12%	4%	25%	3%
86	Ph	2-furyl	Et	47%	33%	52.1 ± 1.1	22%
87	Ph	2-furyl	<i>i</i> -Pr	39%	27%	25.3 ± 0.5	39%
88	Ph	3-furyl	Et	24%	19%	60.4 ± 1.6	10%
89	Ph	3-furyl	<i>i</i> -Pr	33%	42%	58.2 ± 2.1	22%
90	Ph	2-thienyl	Et	3%	1%	2%	15%
91	Ph	2-thienyl	<i>i</i> -Pr	41%	2%	31%	2%
92	Ph	3-thienyl	Et	9%	8%	25%	1%
93	Ph	3-thienyl	<i>i</i> -Pr	3%	4%	1%	2%
94		2-furyl	Et	32%	7%	3%	4%
95		2-furyl	<i>i</i> -Pr	46%	5%	3630 ± 12	1%
96		3-furyl	Et	1%	2%	4%	8%
97		3-furyl	<i>i</i> -Pr	2%	6%	43%	13%
98		2-thienyl	Et	4%	5%	3%	25%
99		2-thienyl	<i>i</i> -Pr	1%	1%	25%	16%
100		3-thienyl	Et	1%	2%	33%	18%
101		3-thienyl	<i>i</i> -Pr	1%	1%	51%	21%
ISAM-140	-	-	-	20%	25%	3.49 ± 0.2	20%
DPCPX	-	-	-	2.20 ± 0.2	157 ± 3	73.24 ± 1.4	1722 ± 11
ZM241385	-	-	-	683 ± 4	1.9 ± 0.1	65.7 ± 1.1	863 ± 4
NECA	-	-	-	14.0 ± 1	20.0 ± 3	2400 ± 35	6.20 ± 9

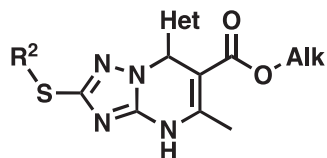
^a Displacement of specific [³H]DPCPX binding in human CHO cells expressed as K_i in nM (n = 3) or percentage displacement of specific binding at a concentration of 1 μM (n = 2).

^b Displacement of specific [³H]4-(2-[7-amino-2-(2-furyl)[1,2,4]triazolo[2,3-a][1,3,5]triazin-5-ylamino]ethyl)phenol binding in human HeLa cells expressed as K_i in nM (n = 3) or percentage displacement of specific binding at a concentration of 1 μM (n = 2).

^c Displacement of specific [³H]DPCPX binding in human HEK-293 cells expressed as K_i in nM (n = 3) or percentage displacement of specific binding at a concentration of 1 μM (n = 2).

^d Displacement of specific [³H]NECA binding in human HeLa cells expressed as K_i in nM (n = 3) or percentage displacement of specific binding at a concentration of 1 μM (n = 2). |

Table 6
Structure and adenosine receptor binding affinities of series XII-XIV.



Series XII: Compounds 102-109

Series XIII: Compounds 110-117

Series XIV: Compounds 118-125

Comp.	R ²	Het	Alk	K _i (nM) or % at 1 μM			
				hA ₁ ^{a)}	hA _{2A} ^{b)}	hA _{2B} ^{c)}	hA ₃ ^{d)}
102	H	2-furyl	Et	1%	2%	9%	3%
103	H	2-furyl	<i>i</i> -Pr	2%	2%	17%	3%
104	H	3-furyl	Et	2%	10%	2%	6%
105	H	3-furyl	<i>i</i> -Pr	2%	2%	3%	1%
106	H	2-thienyl	Et	28%	19%	9%	1%
107	H	2-thienyl	<i>i</i> -Pr	2%	4%	2%	11%
108	H	3-thienyl	Et	9%	2%	3%	13%
109	H	3-thienyl	<i>i</i> -Pr	2%	3%	7%	4%
110	Me	2-furyl	Et	10%	13%	49.2 ± 1.6	9%
111	Me	2-furyl	<i>i</i> -Pr	8%	6%	17.3 ± 0.6	18%
112	Me	3-furyl	Et	2%	24%	123 ± 2	1%
113	Me	3-furyl	<i>i</i> -Pr	1%	3%	29.2 ± 1.1	6%
114	Me	2-thienyl	Et	2%	9%	15%	9%
115	Me	2-thienyl	<i>i</i> -Pr	6%	6%	22%	15%
116	Me	3-thienyl	Et	3%	4%	722 ± 4	23%
117	Me	3-thienyl	<i>i</i> -Pr	5%	1%	17%	2%
118	Bn	2-furyl	Et	20%	4%	4%	15%
119	Bn	2-furyl	<i>i</i> -Pr	1%	2%	9%	3%
120	Bn	3-furyl	Et	6%	5%	19%	12%
121	Bn	3-furyl	<i>i</i> -Pr	16%	21%	6%	20%
122	Bn	2-thienyl	Et	3%	4%	4%	2%
123	Bn	2-thienyl	<i>i</i> -Pr	1%	3%	2%	5%
124	Bn	3-thienyl	Et	10%	11%	8%	3%
125	Bn	3-thienyl	<i>i</i> -Pr	5%	3%	14%	10%
ISAM-140	-	-	-	20%	25%	3.49 ± 0.2	20%
DPCPX	-	-	-	2.20 ± 0.2	157 ± 3	73.24 ± 1.4	1722 ± 11
ZM241385	-	-	-	683 ± 4	1.9 ± 0.1	65.7 ± 1.1	863 ± 4
NECA	-	-	-	14.0 ± 1	20.0 ± 3	2400 ± 35	6.20 ± 9

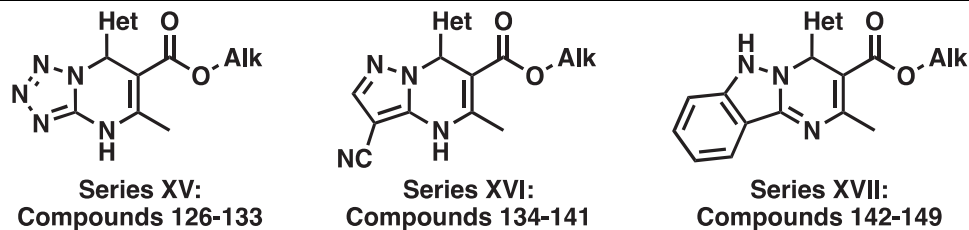
^a Displacement of specific [³H]DPCPX binding in human CHO cells expressed as K_i in nM (n = 3) or percentage displacement of specific binding at a concentration of 1 μM (n = 2).

^b Displacement of specific [³H]4-(2-[7-amino-2-(2-furyl)[1,2,4]triazolo[2,3-*a*][1,3,5]triazin-5-ylamino]ethyl)phenol binding in human HeLa cells expressed as K_i in nM (n = 3) or percentage displacement of specific binding at a concentration of 1 μM (n = 2).

^c Displacement of specific [³H]DPCPX binding in human HEK-293 cells expressed as K_i in nM (n = 3) or percentage displacement of specific binding at a concentration of 1 μM (n = 2).

^d Displacement of specific [³H]NECA binding in human HeLa cells expressed as K_i in nM (n = 3) or percentage displacement of specific binding at a concentration of 1 μM (n = 2). |

Table 7
Structure and adenosine receptor binding affinities of series XV-XVII.



Comp.	Het	Alk	K _i (nM) or % at 1 μM			
			hA ₁ ^{a)}	hA _{2A} ^{b)}	hA _{2B} ^{c)}	hA ₃ ^{d)}
126	2-furyl	Et	4%	3%	511 ± 8	2%
127	2-furyl	<i>i</i> -Pr	6%	4%	257 ± 3	5%
128	3-furyl	Et	6%	5%	23%	13%
129	3-furyl	<i>i</i> -Pr	11%	2%	102	13%
130	2-thienyl	Et	16%	6%	7%	16%
131	2-thienyl	<i>i</i> -Pr	3%	2%	12%	8%
132	3-thienyl	Et	2%	5%	29%	9%
133	3-thienyl	<i>i</i> -Pr	1%	2%	482 ± 6	11%
134	2-furyl	Et	13%	3%	6%	3%
135	2-furyl	<i>i</i> -Pr	12%	3%	9%	9%
136	3-furyl	Et	20%	2%	1%	1%
137	3-furyl	<i>i</i> -Pr	11%	6%	1%	2%
138	2-thienyl	Et	1%	5%	7%	1%
139	2-thienyl	<i>i</i> -Pr	3%	5%	1%	11%
140	3-thienyl	Et	12%	4%	5%	3%
141	3-thienyl	<i>i</i> -Pr	16%	3%	1%	4%
142	2-furyl	Et	5%	2%	39%	15%
143	2-furyl	<i>i</i> -Pr	10%	9%	23%	1%
144	3-furyl	Et	32%	22%	31%	22%
145	3-furyl	<i>i</i> -Pr	8%	3%	24%	11%
146	2-thienyl	Et	2%	1%	17%	16%
147	2-thienyl	<i>i</i> -Pr	3%	9%	26%	11%
148	3-thienyl	Et	18%	6%	17%	8%
149	3-thienyl	<i>i</i> -Pr	19%	9%	19%	1%
ISAM-140	-	-	20%	25%	3.49 ± 0.2	20%
DPCPX	-	-	2.20 ± 0.2	157 ± 3	73.24 ± 1.4	1722 ± 11
ZM241385	-	-	683 ± 4	1.9 ± 0.1	65.7 ± 1.1	863 ± 4
NECA	-	-	14.0 ± 1	20.0 ± 3	2400 ± 35	6.20 ± 9

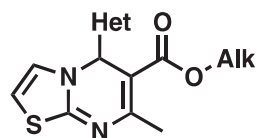
^a Displacement of specific [³H]DPCPX binding in human CHO cells expressed as K_i in nM (n = 3) or percentage displacement of specific binding at a concentration of 1 μM (n = 2).

^b Displacement of specific [³H]4-(2-[7-amino-2-(2-furyl)[1,2,4]triazolo[2,3-a][1,3,5]triazin-5-ylamino]ethyl)phenol binding in human HeLa cells expressed as K_i in nM (n = 3) or percentage displacement of specific binding at a concentration of 1 μM (n = 2).

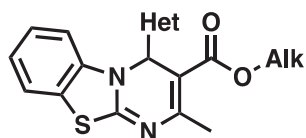
^c Displacement of specific [³H]DPCPX binding in human HEK-293 cells expressed as K_i in nM (n = 3) or percentage displacement of specific binding at a concentration of 1 μM (n = 2).

^d Displacement of specific [³H]NECA binding in human HeLa cells expressed as K_i in nM (n = 3) or percentage displacement of specific binding at a concentration of 1 μM (n = 2).

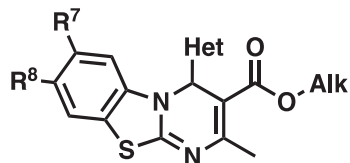
Table 8
Structure and adenosine receptor binding affinities of series XVIII-XXI.



Series XVIII:
Compounds 150-157



Series XIX:
Compounds 158-165



Series XX: Compounds 166-173
Series XXI: Compounds 174-181

Comp.	R ⁷	R ⁸	Het	Alk	K _i (nM) or % at 1 μM			
					hA ₁ ^{a)}	hA _{2A} ^{b)}	hA _{2B} ^{c)}	hA ₃ ^{d)}
150	-	-	2-furyl	Et	24%	7%	15%	1%
151	-	-	2-furyl	<i>i</i> -Pr	1%	1%	15%	4%
152	-	-	3-furyl	Et	20%	2%	27%	12%
153	-	-	3-furyl	<i>i</i> -Pr	2%	3%	43%	4%
154	-	-	2-thienyl	Et	14%	4%	3%	5%
155	-	-	2-thienyl	<i>i</i> -Pr	7%	3%	10%	3%
156	-	-	3-thienyl	Et	16%	2%	17%	4%
157	-	-	3-thienyl	<i>i</i> -Pr	11%	8%	22%	3%
158 (ISAM-J1877)	-	-	2-furyl	Et	24%	29%	9.4 ± 0.4	4%
159 (ISAM-MM42)	-	-	2-furyl	<i>i</i> -Pr	1%	16%	11.6 ± 0.8	5%
160 (ISAM-J1878)	-	-	3-furyl	Et	17%	47%	8.6 ± 0.3	6%
161 (ISAM-MM44)	-	-	3-furyl	<i>i</i> -Pr	5%	33%	9.1 ± 0.4	1%
162	-	-	2-thienyl	Et	6%	3%	138 ± 2	6%
163	-	-	2-thienyl	<i>i</i> -Pr	3%	1%	214 ± 4	2%
164 (ISAM-J1881)	-	-	3-thienyl	Et	1%	4%	11.2 ± 0.8	3%
165 (SY1MM-45)	-	-	3-thienyl	<i>i</i> -Pr	2%	8%	44.2 ± 0.4	1%
166	Cl	H	2-furyl	Et	34%	36%	76.7 ± 1.2	2&
167	Cl	H	2-furyl	<i>i</i> -Pr	1%	1%	48%	4%
168	Cl	H	3-furyl	Et	2%	2%	65.4 ± 2.2	2%
169	Cl	H	3-furyl	<i>i</i> -Pr	3%	23%	99.2 ± 1.2	12%
170	Cl	H	2-thienyl	Et	13%	11%	14%	27%
171	Cl	H	2-thienyl	<i>i</i> -Pr	14%	12%	8%	6%
172	Cl	H	3-thienyl	Et	8%	10%	37.1 ± 2.1	11%
173	Cl	H	3-thienyl	<i>i</i> -Pr	8%	2%	12%	1%
174	H	Cl	2-furyl	Et	13%	43%	14.5 ± 0.6	17%
175	H	Cl	2-furyl	<i>i</i> -Pr	2%	15%	30.8 ± 0.5	1%
176 (ISAM-H143)	H	Cl	3-furyl	Et	20%	90.7 ± 4	4.30 ± 0.2	3%
177 (ISAM-H144)	H	Cl	3-furyl	<i>i</i> -Pr	8%	49%	10.2 ± 0.9	5%
178	H	Cl	2-thienyl	Et	18%	29%	61.4 ± 2.1	10%
179	H	Cl	2-thienyl	<i>i</i> -Pr	5%	21%	165 ± 4	8%
180	H	Cl	3-thienyl	Et	1%	5%	77.2 ± 1.6	5%
181	H	Cl	3-thienyl	<i>i</i> -Pr	4%	20%	52.8 ± 1.3	1%
ISAM-140	-	-	-	-	20%	25%	3.49 ± 0.2	20%
DPCPX	-	-	-	-	2.20 ± 0.2	157 ± 3	73.24 ± 1.4	1722 ± 11
ZM241385	-	-	-	-	683 ± 4	1.9 ± 0.1	65.7 ± 1.1	863 ± 4
NECA	-	-	-	-	14.0 ± 1	20.0 ± 3	2400 ± 35	6.20 ± 9

^a Displacement of specific [³H]DPCPX binding in human CHO cells expressed as K_i in nM (n = 3) or percentage displacement of specific binding at a concentration of 1 μM (n = 2).

^b Displacement of specific [³H]4-(2-[7-amino-2-(2-furyl)[1,2,4]triazolo[2,3-*a*][1,3,5]triazin-5-ylamino]ethyl)phenol binding in human HeLa cells expressed as K_i in nM (n = 3) or percentage displacement of specific binding at a concentration of 1 μM (n = 2).

^c Displacement of specific [³H]DPCPX binding in human HEK-293 cells expressed as K_i in nM (n = 3) or percentage displacement of specific binding at a concentration of 1 μM (n = 2).

^d Displacement of specific [³H]NECA binding in human HeLa cells expressed as K_i in nM (n = 3) or percentage displacement of specific binding at a concentration of 1 μM (n = 2).

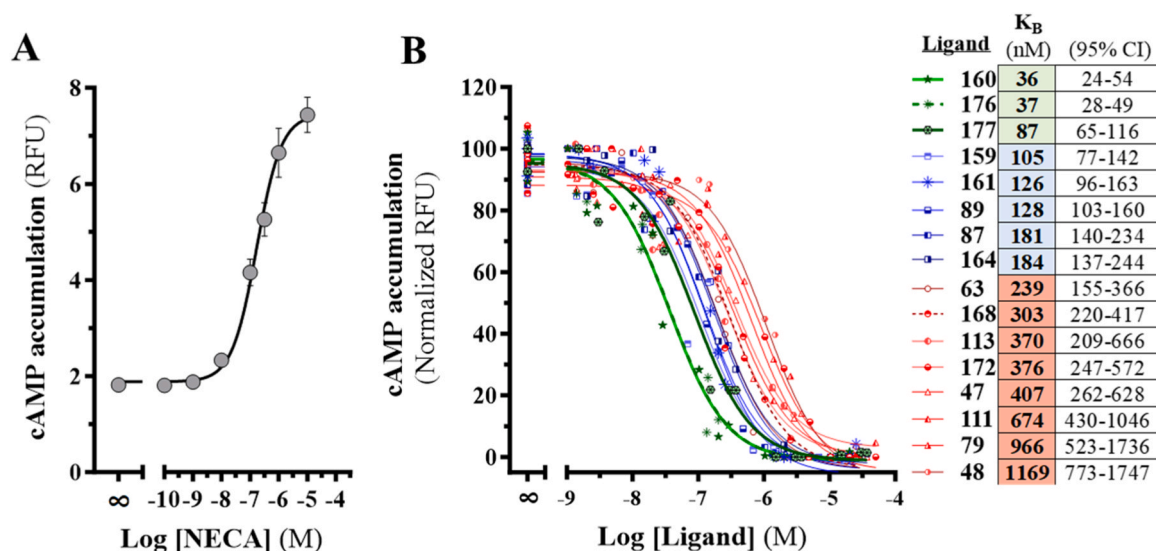


Fig. 3. Blockade of A_{2B}R-mediated cAMP accumulation. (A) Determination of NECA-mediated cAMP accumulation in A_{2B}AR cells. Cells were incubated in the absence or presence of increasing concentrations of NECA, and the cAMP accumulation determined. Results are expressed as relative TR-FRET units (RFU; see *Experimental section*). (B) cAMP accumulation in A_{2B}AR cells stimulated with NECA (300 nM) in the absence or presence of increasing concentrations of 47, 48, 63, 79, 87, 89, 111, 113, 159, 160, 161, 164, 168, 172, 176, and 177. For simplicity, the mean of three independent experiments performed in quadruplicate is shown for each ligand. The K_B values were calculated using the pooled data of all three experiments (see *Materials and Methods*).

evaluation of compounds as a racemic mixture. However, the structural modeling is based on the previously defined stereospecific binding mode, considering the predicted eutomer, which was further confirmed also for this series in the next section.

The biological evaluation of the 168 compounds revealed 25 ligands with attractive A_{2B}AR affinity (K_i < 100 nM) and selectivity (> 1000-fold), of which nine ligands exhibit exceptional A_{2B}AR affinity (K_i < 25 nM) [e.g., compounds 111 (Table 6), 158, 159, 160, 161, 164, 174, 176, 177 (Table 8)]. The available data show clear SAR trends, with benzo[4,5]thiazolo[3,2-a]pyrimidine (and its 8-chlorine derivatives) being the most relevant A_{2B}AR antagonists here obtained from quantitative and qualitative points of view [series XIX and XXI (Table 8)].

A comparative analysis of the binding data obtained from the 2-aminosubstituted pyrimidine derivatives (series I-VII, Tables 2-4) and from the corresponding series of monocyclic model derivatives (Table 1) shows that the bicyclic ring opening strategy, which leads to mono- (or di-) substituted amines at position 2, has a negative impact on the A_{2B}AR affinity: 2-methylamino, 2,2-dimethylamino, 2-phenylamino and 2-acetamido monocyclic derivatives (series I-IV) are inactive, while only 9 over 56 ligands from the remaining series V-VII show measurable A_{2B}AR binding affinity (K_i = 83.5 – 480 nM). In general, these data show same trend previously described in the early series I-III, where the best combination of substituents is 2-furyl as heteroaromatic ring (Het) and isopropyl as alkoxy residue in the ester moiety (Alk) [e.g., compounds 47 (series V, Table 6), 55 (series VI, Table 7) and 63 (series VII, Table 8)]. Analysis of the docking poses suggested that the main interactions of the 2-aminosubstituted monocycles with the A_{2B}AR could be strongly influenced by the tautomeric form considered, with tautomer III (bearing an exocyclic imine group, Fig. 4) being the only tautomer that could establish a double hydrogen bond with Asn254^{6,55}. On the contrary, the tautomer I (Fig. 4) could only establish one H-bond while presenting the protonated N1 of the monocycle facing the NH of the amide group of Asn254^{6,55}, in a clearly unfavorable electrostatic orientation. Finally, the alternative tautomer II (Fig. 4) could only establish H-bond interactions with Asn254^{6,55} if the amide sidechain of this key residue would be flipped, which is energetically unfavorable based on the rotamer population observed in all experimental structures of adenosine receptors, further supported by our free energy calculations [20].

The concept that the exocyclic imine form (Fig. 4A, tautomer III) represents the bioactive conformation was supported by previous series (Fig. 1, ligands 7) and further reinforced by the energetic preference for this tautomer, as determined through quantum mechanical calculations in continuous solvent and FEP simulations comparing the two conformations' affinity for the A_{2B}AR (Supplementary Figure S1).

Based on these indications, we decided to determine the major tautomeric form of the monocyclic series (I-VII) using a combination of NMR techniques. The multiplicity of the signal corresponding to the proton at C4 (Fig. 4A) was initially analysed using conventional ¹H NMR techniques. A singlet is indicative of the predominancy of tautomer I, while a doublet would reveal coupling with a proton at N3 (as in tautomers II or III, Fig. 4A) as previously reported for 2-cyanoiminopyrimidines [21]. To differentiate between them, ROESY experiments were conducted by irradiating the typical methyl group of these structures (C7, Fig. 4B).²¹ Molecules with the protonated tautomeric form at N1 will exhibit ROESY effect when the hydrogen atoms are within 3 Å, a behaviour that cannot occur if the protonated nitrogen is N2 (Fig. 4B). The experimental observations were elucidated based on the modeled binding poses, with representant compounds of inactive series [series I (R = Me, R' = H), series II, (R = R' = Me), series III (R = Ph, R' = H) and series IV (R = COMe, R' = H)] all showing a diamine tautomer II as the major form (Fig. 4A, diamine N1H). In contrast, compounds from the active series V (R = COPh, R' = H) and VI (R = SO₂Ph, R' = H) adopt the tautomer III form, compatible with a double hydrogen bond with Asn254^{6,55} (Fig. 4B-C, tautomer III). Interestingly, series VII prefers for the diamine-type tautomer I, stabilized by a predicted internal hydrogen bond between N3 in the monocycle and the NH of the benzimidazole. Consequently, binding mode studies for this series complemented the experimental data, enabling the establishment of 2 or even 3 hydrogen bonds with Asn254^{6,55}, which could explain the moderate affinity (e.g., ligand 63, K_i = 127 nM, Fig. 4).

To further confirm our binding mode hypothesis, we conducted FEP simulations between the representative compounds of each series. We used the same protocol as in previous studies to determine relative binding free energy shifts (ΔΔG_{bind}, kcal/mol) due to chemical substitutions [18], the results being summarized in Fig. 5A. Compounds selected for these calculations maintained the substituents invariable on Het = 2-furyl and Alk = *i*-Pr, and considered only the most stable

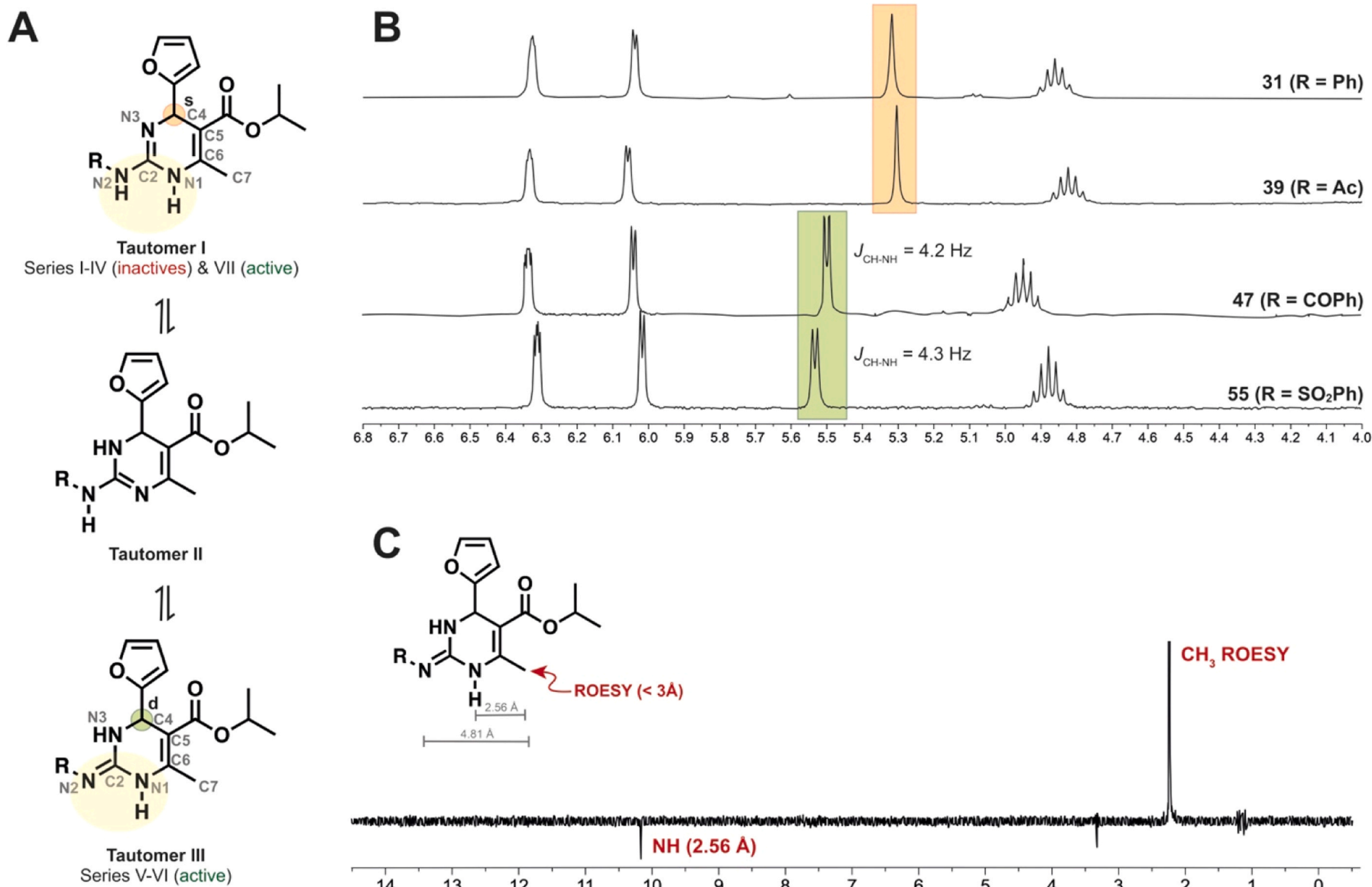


Fig. 4. A) Different possible tautomers for the monocyclic series in DMSO- d_6 . In yellow: zone of double hydrogen bond interaction with Asn^{6,55} B) ^1H NMR peaks (4.0 – 6.8 ppm) for inactive compounds **31** and **39**; and active compounds **47** and **55**. Singlet at ~5.3 ppm (orange) confirms C2-N3 double bond (diamine form), while doublet at ~5.5 ppm (green) could be a C2-N2 (Tautomer III) or C2-N1 (Tautomer II) double bond. C) ROESY example of CH₃ (C7) irradiation. It is only possible to see the ROESY effect (< 3 Å) if the protonated nitrogen is N1, confirming C2-N2 imine tautomeric state (tautomer III).

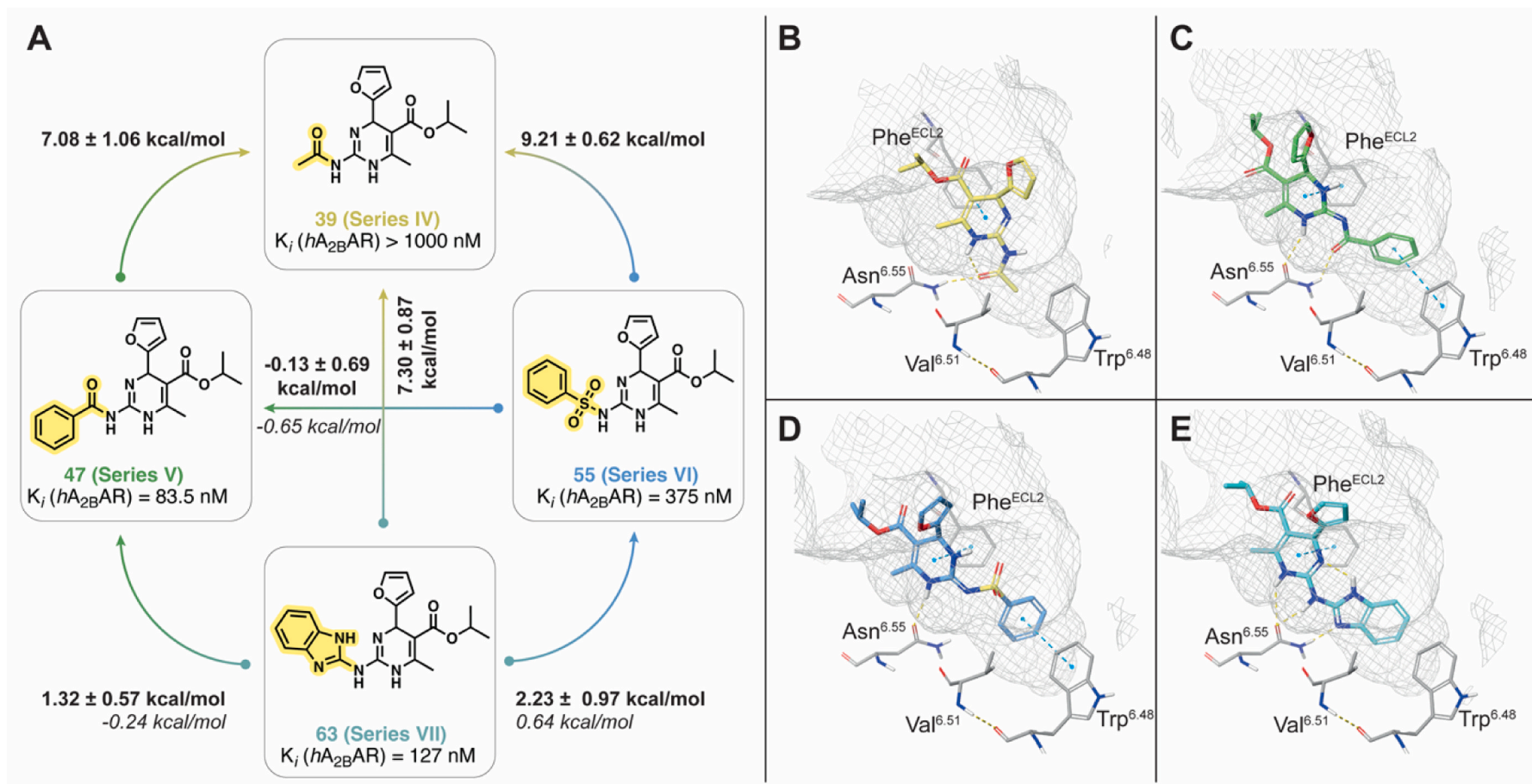


Fig. 5. A) FEP cycle for representative monocycles, showing FEP calculated relative affinities in bold (following the direction of the transformation indicated by the arrow, with associated s.e.m. values). When the experimental K_i is available for the pair of compounds implicated, the corresponding experimental shift in affinities is indicated (regular font). B) Binding mode of 39 (series IV), C) 47 (series V), D) 55 (series VI) and E) 63 (series VII). Yellow marked structures indicate the changing atoms between FEP pairwise simulations; grey mesh represent the volume of the $A_{2B}AR$ binding site. Yellow dashed lines: hydrogen bonds, blue dashed lines: π - π interactions, orange dashed lines: bad contacts.

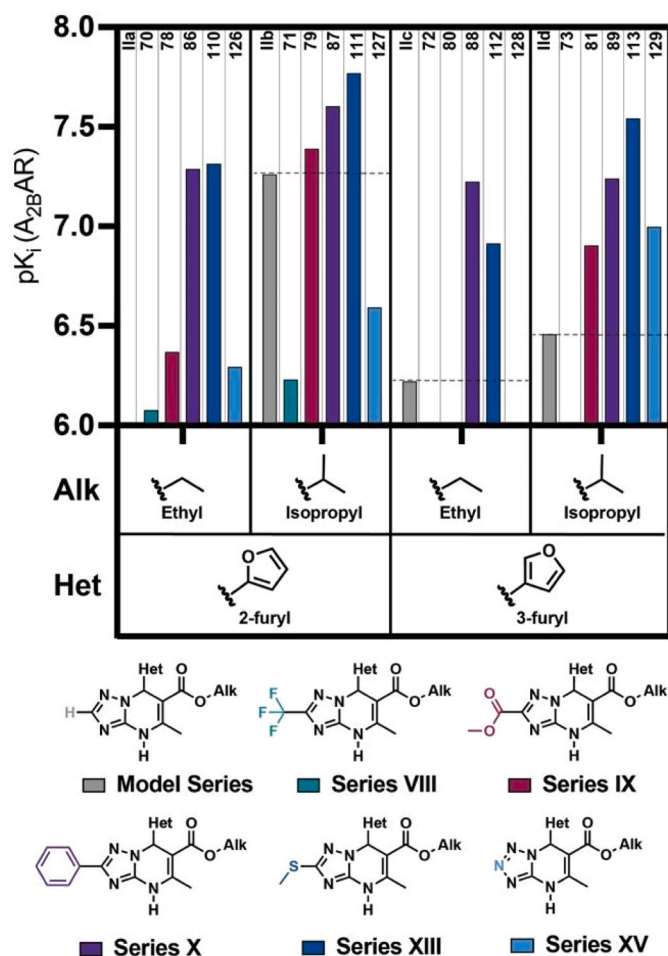


Fig. 6. Interleaved bars chart showing $A_{2B}AR$ pK_i $[-\log(K_i)]$ for bicyclic series showing $A_{2B}AR$ binding affinity (VIII-X, XIII, XV, XVI-XVII) and for model series II as a reference (grey bars). Compounds with thienyl as a heterocyclic residue are not shown in this graph as they have no relevant affinity.

tautomer in each case (Fig. 5A). Perturbations involved at least one compound with measurable affinity ($K_i < 1 \mu M$) were carried, and compound 39 (series IV, $R_2 = COMe$) was used as a reference inactive compound (Fig. 5B). The computations reproduce the moderate affinity of series V (compound 47, $R_2 = COPh$) compared to the inactive series IV. This is explained by an additional π - π stacking interaction modeled between the phenyl and Trp247^{6,48}, while preserving a double H-bond with Asn254^{6,55} via the carbonyl group. A similar behaviour is observed for compounds in series VI (compound 55, $R^2 = SO_2Ph$), and the model is qualitatively sensitive to the three-fold difference with respect to series V ($\Delta\Delta G_{bind} < 1$ kcal/mol, both experimental and calculated). The slight improvement observed for series VII (compound 63) is exaggerated by the FEP simulations, the reason being located on the aminoindole substituent allowing multiple H-bonds with the receptor (Fig. 5B). An interesting observation from the FEP simulations is that the binding mode of series V-VII is shifted compared to series IV and also to previously modeled monocyclic series [10]. The reason for this can be attributed to the accommodation of the bulky aromatic substituent in R^2 within the deeper region of the receptor, resulting in substituents in R^4 and R^5 occupying different regions on the binding site (Fig. 5B-E). The corresponding alchemical transformation of any representative compound belonging to series V-VII into compound 39 (series IV) results in a remarkable predicted loss of affinity ($\Delta\Delta G_{bind}$ 5.0–7.7 kcal/mol), in qualitative consistent with the complete inactivity of this molecule and supporting the validity of these models. The pairwise binding affinity

differences between compounds 47, 55 and 63 (representatives of series V, VI and VI, respectively) have been calculated for all possible combinations, allowing estimation of the cycle closure error corresponding to the pathway $63 \rightarrow 55 \rightarrow 47 \rightarrow 63$, which is remarkably close to the theoretical zero (accumulated $\Delta\Delta G_{bind} = 0.82$ kcal/mol).

The adenosinergic profile obtained for the family of 2-substituted bicyclic compounds (series VIII-XIV) and for the different bioisosteric replacements of bi- and tricyclic compounds (series XV-XIX) is summarized in Fig. 6. Only compounds containing a furyl group on the stereogenic center maintain affinity for the $A_{2B}AR$ ($K_i = 17.3 - 3630$ nM), showing that the trend observed for previous series is independent of the scaffold, except for the low affinity thienyl derivatives 116 (series XIII, $K_i = 722$ nM) and 133 (series XV, $K_i = 482$ nM). For the SAR study, $A_{2B}AR$ affinity data of each series' representative were plotted alongside the corresponding values of the analogous compound in model series II (Fig. 6). Functionalization of position 2 of the model series II (Alkyl 7-heteroaryl-5-methyl-4,7-dihydro-[1,2,4]triazolo[1,5- α]pyrimidine-6-carboxylates) with carbon-based groups emerged as a good strategy, with the exception of trifluoromethyl derivatives (series VIII). The methoxycarbonyl and phenyl substituents explored in series IX-X showed several molecules with K_i for the $A_{2B}AR$ below 100 nM, improving the moderate affinities of model series II (Fig. 6). The best compounds combined 2-furyl as heteroaromatic ring (Het) and isopropyl as an alkoxy residue in the ester moiety (Alk) [e.g., 71, 79, 87], as previously observed for monocyclic compounds. In series XI-XIV, we explored substituting position 2 with heteroatom-based groups (*N*-methylpiperazine, thiol, methylthiol and benzylthiol). Docking the representative compound revealed that the *N*-methylpiperazine in series XI occupies an unfavored region for such a charged moiety, i.e., near Trp247^{6,48}, and attempts to dock the inactive benzylthiol derivative in series XIV failed. The comparison between the thiol and methylthiol substitutions (series XII and XIII) is particularly intriguing. The apparent small change in a methyl group is indeed causing a systematic recovery of the binding affinity of the series, in particular for the furyl-containing compounds. The reason is not evident from a direct comparison of the corresponding docking poses, and instead we rationalized this trend based on the high ionizable potential of the -SH group in series XII. Quantum mechanical calculations reveal a pK_a of 3.54 for compound 103 ($m062x/6-311+g(d,p)$ level of theory with thiophenol as the reference base) suggesting that these compounds exist as anions under physiological conditions. According to our binding model, the charge would disrupt binding to the receptor modelled for series XIII where $R^2 = SMe$ (Supplementary Figure S2F-G). Indeed, the last series contains some of the most interesting bicyclic compounds, in most cases importantly improving the affinity of the corresponding analogues in model series II [e.g., 110 ($K_i = 49.2$ nM) vs IIa (inactive), 111 ($K_i = 17.3$ nM) vs IIb ($K_i = 55.6$ nM), 112 ($K_i = 123$ nM) vs IIc ($K_i = 602$ nM) and 113 ($K_i = 29.2$ nM) vs IID ($K_i = 350$ nM)]. Overall, the $A_{2B}AR$ affinity profile of series VIII-XIV aligns with the predicted binding mode (Supplementary Figure S2A-J). The double hydrogen bond with Asn254^{6,55} and π - π interactions between the core and Phe168^{ECL2}, would be complemented by the optimal substitutions at C_2 (e.g., methoxycarbonyl, phenyl and methylthio- substituents) reaching Trp247^{6,48} and further stabilizing receptor binding.

Bioisosteric exploration for model series II and III was conducted in series XV-XXI, as depicted in Supplementary Figure S3. Series XV, based on the classical replacement of triazole by tetrazole, demonstrated only marginal affinity improvements (e.g., 129, Fig. 6). Series XVI evidenced that replacing N3, engaged in interactions with Asn254^{6,55}, with an exocyclic cyano group has a negative impact on binding. Series XVII, which explores the inversion of the tricyclic structure, resulted in inactive compounds across all four ARs subtypes. Despite unsuccessful attempts to dock compound 143, the series was analyzed with the hope that the predominant tautomer, similar to monocycles, might convert into bioactive form upon interaction with the binding site.

Finally, replacing nitrogen with sulfur in bi- and tricyclic scaffolds to

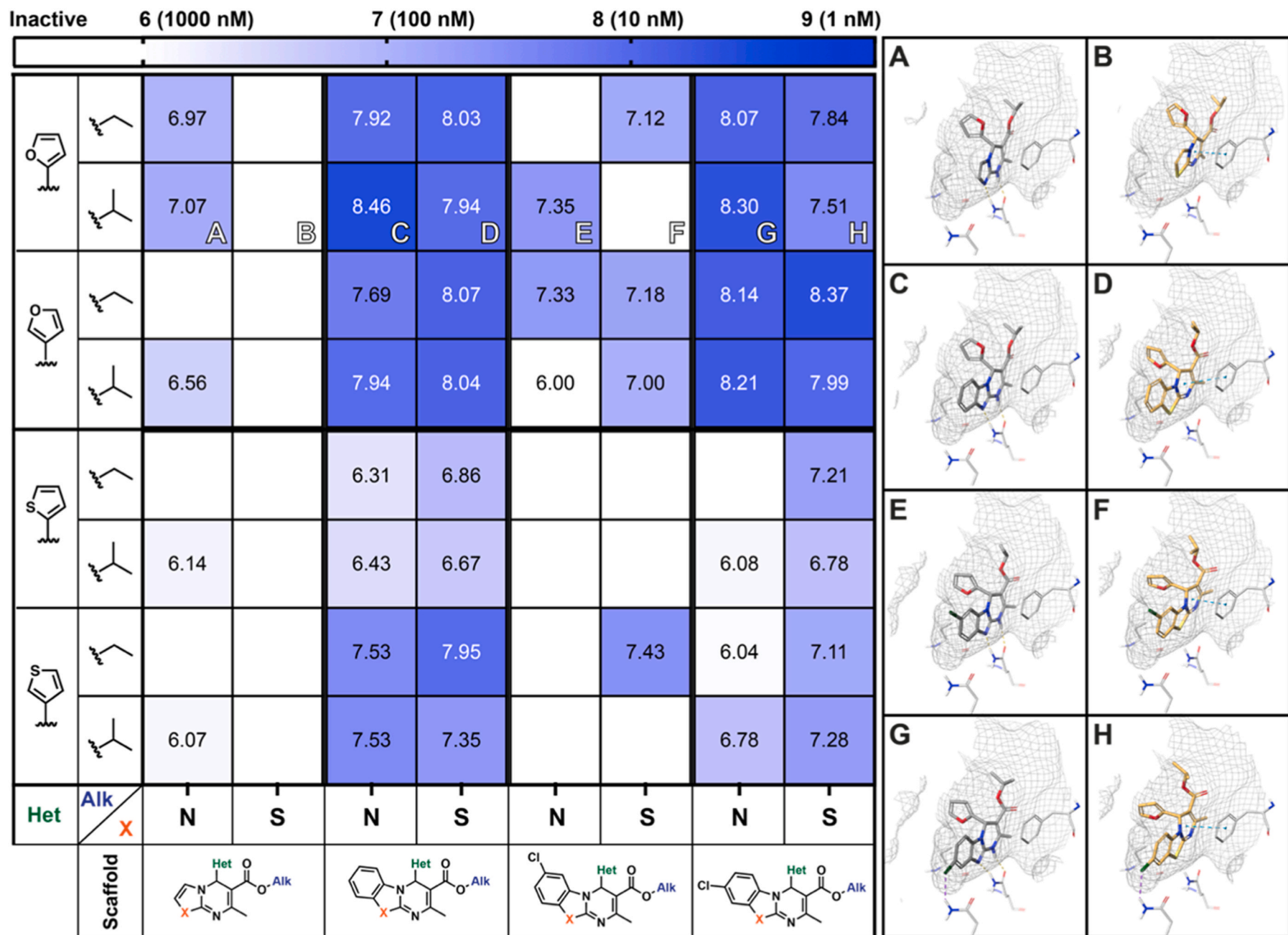


Fig. 7. Heatmap chart showing $A_{2B}AR$ pK_i [$-\log(K_i)$] for series XIX-XXI (S columns) compared with previously published dihydrobenzo[4,5]imidazo[1,2-a]pyrimidines analogues (N columns). Docking pose for enantiomers of A) 8b [17] B) 151 (series XVIII), C) 9a [17] (ISAM-140, Model series III), D) 159 (ISAM-MM42, series XIX), E) 9b [18], F) 167 (series XX) G) 9c [18], and H) 175 (series XXI). Receptor is $A_{2B}AR$ homology model from $A_{2A}AR$ (PDB: 3EML), and grey mesh represent $A_{2B}AR$ binding site.

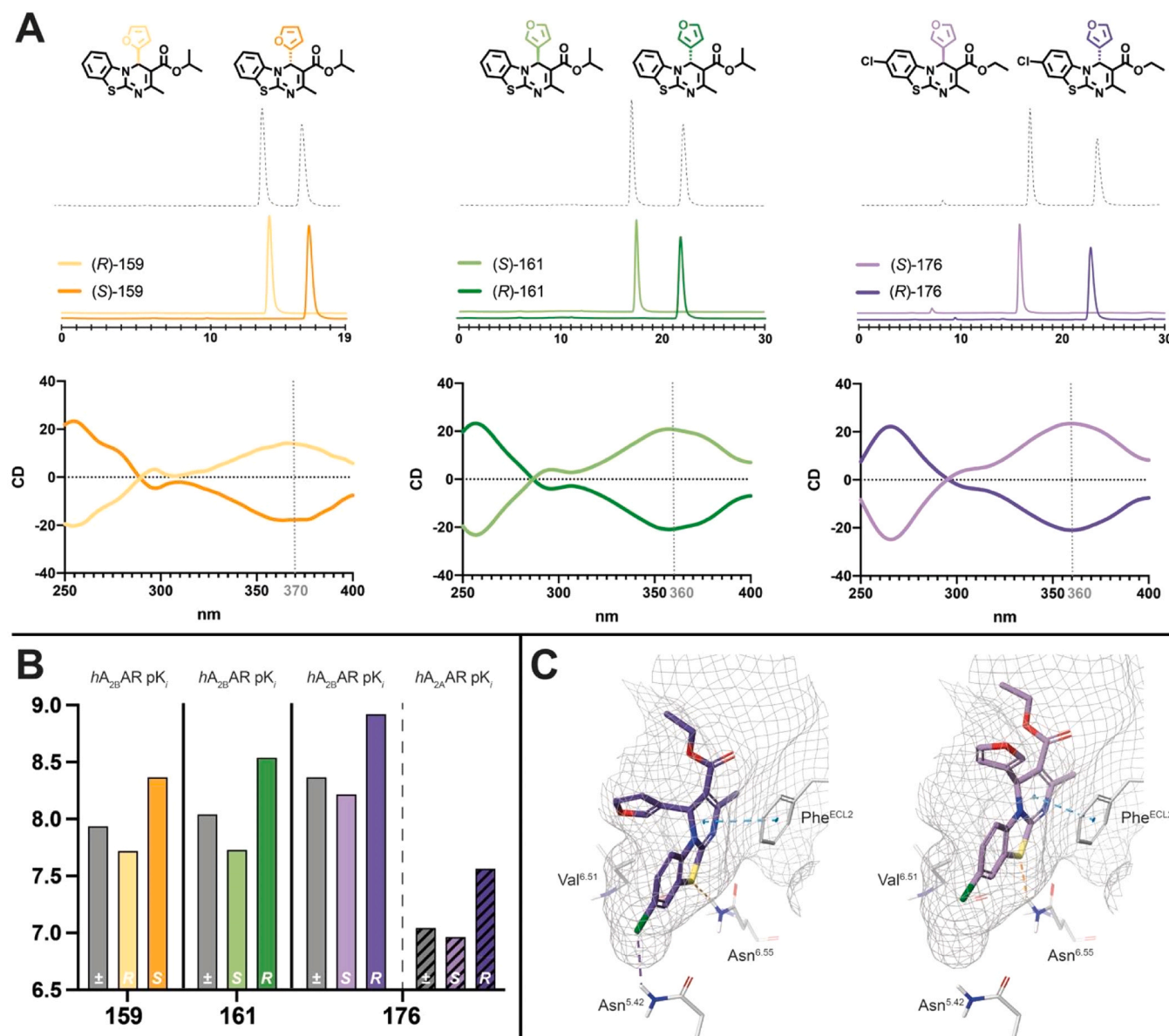


Fig. 8. Enantiospecific binding to A_{2B} and $A_{2A}AR$. **A**) Chiral HPLC traces and circular dichroism spectra of selected racemic ligands (159, 161, 176) and their enantiomers. **B**) Interleaved bar chart showing A_{2A} (pattern fill) and $A_{2B}AR$ (solid fill) pK_i for racemic mixtures (grey), distomers (light coloured) and eutomers (dark coloured). **C**) Binding mode of (R)-176 (eutomer, left) and (S)-176 (distomer, right). Receptor is $A_{2B}AR$ homology model from $A_{2A}AR$ (PDB: 3EML), and grey mesh represent $A_{2B}AR$ binding site. Note that the eutomer fits better in the receptor, forming a halogen bond with Asn^{5.42}, but not in the distomer.

produce thiazole (series XVIII) and benzothiazole derivatives (series XIX-XXI) yielded some of the most potent compounds reported so far within our program and provided crucial evidence for constructing new SAR data for this family of adenosine receptor antagonists. Fig. 7 summarizes the affinity data and the proposed binding modes for thiazole and benzothiazole derivatives, in comparison to their parent imidazole and benzimidazole analogues [17]. The replacement disrupts the formation of a double direct hydrogen bond with Asn254^{6.55}. Surprisingly, the impact on the binding affinity of bicyclic thiazoles are opposed to those observed for tricyclic benzothiazoles: while the thiazole analogues (series XVIII) completely lose the moderate affinity of the parent imidazoles (model series II, Fig. 7 and Table 8, compounds 150–157), most benzothiazoles in series XIX-XXI exhibit an excellent $A_{2B}AR$ antagonist profile (Table 8, compounds 158–181), similar or even better than the parent benzimidazoles (model series III, Fig. 7). Directly comparing the binding affinities of compounds in series XIX to their counterparts in model series III shows an overall positive effect of replacing the benzimidazole with a benzothiazole; in particular for the thiophene

derivatives, where the moderate affinity of the corresponding model compounds IIIe-IIIh ($K_i = 29.34 - 484.6$ nM) increases at least 2-fold (compounds 162–165, $K_i = 11.2 - 214$ nM), while the already excellent profile of furyl derivatives in the model series IIIa-IIIc, ($K_i = 3.49 - 20.6$ nM) is on average maintained in the benzothiazole counterparts (158–165, $K_i = 8.6 - 11.6$ nM). This surprising data aligns with the new binding mode proposed for the tricyclic system, which combines high stability with a certain degree of flexibility (Fig. 7), enabling the insertion of a water molecule between the sulphur and the oxygen in Asn254^{6.55}, underscoring the importance of considering dynamic and solvation effects in computer-assisted structure-based ligand design programs. Conversely, the bicyclic scaffold, already demonstrating weaker binding in the model series (for example, when comparing the affinities of series II and III), is more sensitive to the (imidazole/thiazole) replacement.

Chlorination at position 7 of the benzothiazole derivatives (series XX) negatively affects affinity, similar to trends observed in the benzimidazole series (Fig. 7) [18], with the thiophene-substituted compound

Table 9
Structure and Adenosine Receptor Affinities of Racemic and Enantiomers of Selected Ligands and previous reported related compounds (in grey).

Comp.	K _i (nM) or % at 1 μM			
	hA ₁ ^{a)}	hA _{2A} ^{b)}	hA _{2B} ^{c)}	hA ₃ ^{d)}
(±)-ISAM-140 ¹⁸	20%	25%	3.49 ± 0.2	2%
(R)-ISAM-140 ¹⁸	4%	2%	17%	2%
(S)-ISAM-140 ¹⁸	2%	2%	0.89 ± 0.2	4%
(±)-159 [(±)-ISAM-MM42]	1%	16%	11.6 ± 0.8	5%
(R)-159 [(R)-ISAM-MM42]	26%	10%	19.2 ± 1.2	12%
(S)-159 [(S)-ISAM-MM42]	24%	4%	4.30 ± 0.6	1%
(±)-161 [(±)-ISAM-MM44]	5%	33%	9.1 ± 0.4	1%
(S)-161 [(S)-ISAM-MM44]	18%	8%	18.7 ± 3	3%
(R)-161 [(R)-ISAM-MM44]	6%	44%	2.90 ± 0.4	20%
(±)-ISAM-M89A ¹⁸	37%	176 ± 4	6.10 ± 0.7	25%
(S)-ISAM-M89A ¹⁸	24%	25%	53%	19%
(R)-ISAM-M89A ¹⁸	37%	96.3 ± 6	2.6 ± 0.3	25%
(±)-176 [(±)-ISAM-H143]	20%	90.7 ± 4	4.30 ± 0.2	3%
(S)-176 [(S)-ISAM-H143]	5%	109 ± 6	6.10 ± 0.6	20%
(R)-176 [(R)-ISAM-H143]	1%	27.3 ± 1.8	1.20 ± 0.2	1%
ISAM-140	20%	25%	3.49 ± 0.2	20%
DPCPX	2.20 ± 0.2	157 ± 3	73.24 ± 1.4	1722 ± 11
ZM241385	683 ± 4	1.9 ± 0.1	65.7 ± 1.1	863 ± 4
NECA	14.0 ± 1	20.0 ± 3	2400 ± 35	6.20 ± 9

^a Displacement of specific [³H]DPCPX binding in human CHO cells expressed as K_i in nM (n = 3) or percentage displacement of specific binding at a concentration of 1 μM (n = 2).

^b Displacement of specific [³H]4-(2-[7-amino-2-(2-furyl)[1,2,4]triazolo[2,3-a][1,3,5]triazin-5-ylamino]ethyl)phenol binding in human HeLa cells expressed as K_i in nM (n = 3) or percentage displacement of specific binding at a concentration of 1 μM (n = 2).

^c Displacement of specific [³H]DPCPX binding in human HEK-293 cells expressed as K_i in nM (n = 3) or percentage displacement of specific binding at a concentration of 1 μM (n = 2).

^d Displacement of specific [³H]NECA binding in human HeLa cells expressed as K_i in nM (n = 3) or percentage displacement of specific binding at a concentration of 1 μM (n = 2).

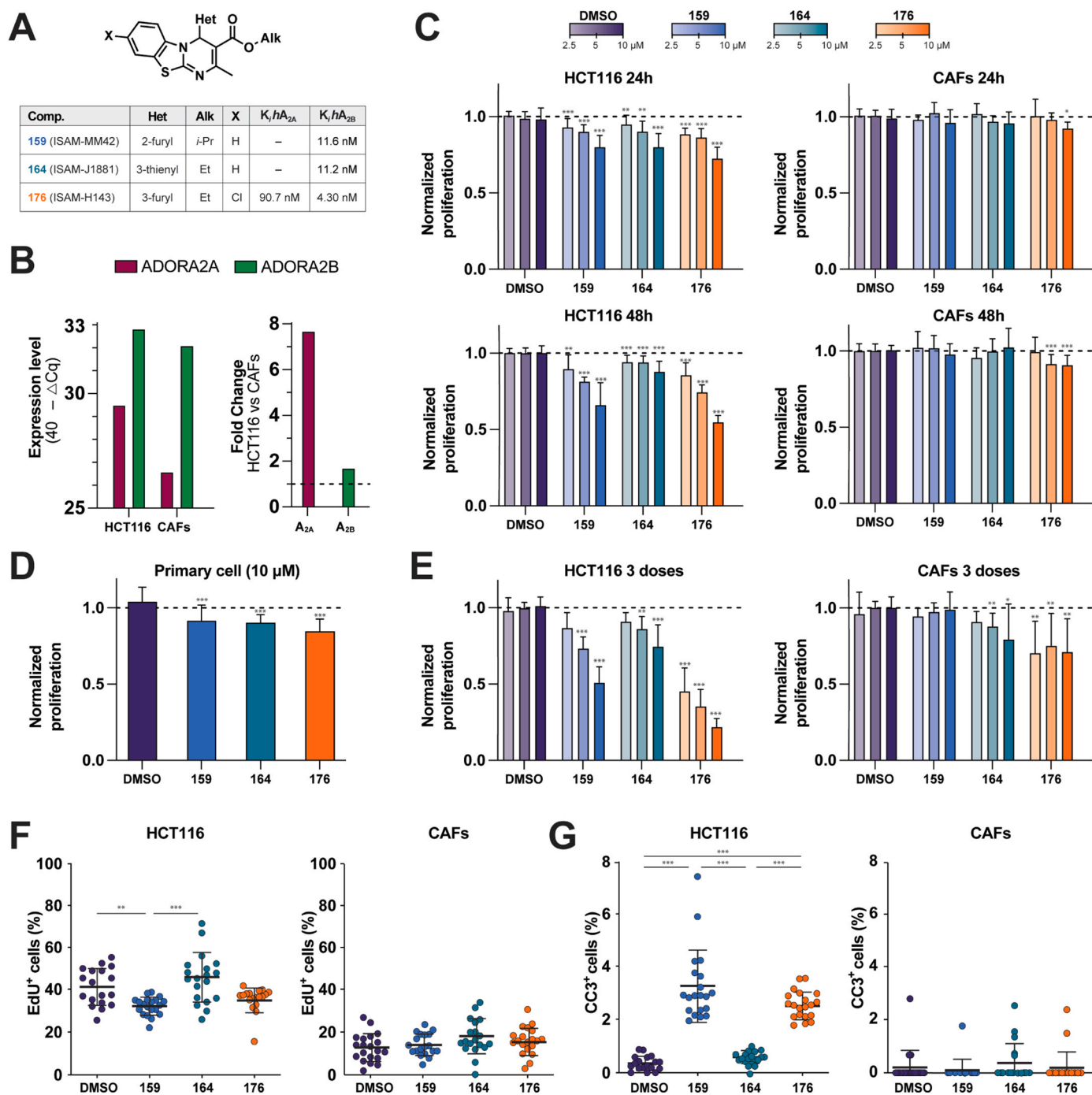


Fig. 9. A) Absolute expression of ADORA2A and ADORA2B on HCT and CAFs using GAPDH as a reference gene and Fold change on expression in HCT116 vs CAFs. B) Structure of selected ligands and affinity binding data for A_2 adenosine receptors. C) Relative cell viability to untreated control HCT116 and CAFs ($n = 12$, mean \pm SD) measured by AlamarBlue assay 24 h and 48 h after treatment. D) Relative cell viability to untreated control of colorectal cancer primary cell line ($n = 12$, mean \pm SD) measured by AlamarBlue assay 48 h after treatment with 10 μ M of antagonists. E) Relative cell viability to untreated control HCT116 and CAFs ($n = 12$, mean \pm SD) measured by AlamarBlue assay after 24 h of three consecutive doses, administered at 24-hour intervals. Statistical analysis ANOVA with Dunnett's multiple comparisons to untreated control was performed with * $p < 0.05$, ** $p < 0.01$, and *** $p < 0.001$. F) EdU positive cells for HCT116 and CAFs ($n = 20$, mean \pm SD). G) CC3 positive cells for HCT116 and CAFs ($n = 20$, mean \pm SD). Statistical analysis Kruskal-Wallis was performed with * $p < 0.05$, ** $p < 0.01$, and *** $p < 0.001$.

172 being the best binder ($A_{2B}AR$ $K_i = 37.1$ nM). Meanwhile, the effect of chlorination at position 8 of the benzothiazole derivatives is better tolerated, even showing marginal improvements in affinity with high $A_{2B}AR$ affinity values for the entire series XXI ($K_i = 4.30 - 165$ nM). Overall, the chlorination effect of benzothiazoles shows a similar pattern to that recently observed in the benzimidazole series (Fig. 7) [18], reinforcing the idea of a conserved binding mode after this replacement, which allows the recently described halogen bond between Asn254^{5,42}

and the chlorine atom at position 8 (Fig. 7H-G) [18]. This is particularly relevant for benzothiazole derivatives with thiophene at R⁴, which, unlike their counterparts in the benzoimidazole series, show noticeable affinity values for the $A_{2B}AR$ ($K_i = 52.8 - 165$ nM). Together, these data support the hypothesis that the structural novelty introduced by benzothiazole scaffold, with its single direct H-bond to Asn254^{6,55}, provides an interesting combination of binding site complementarity with enough flexibility to accommodate groups such as 3-furan or

thiophenes, breaking the negative trend in affinity described for these substituents at Het position in other scaffolds. The behaviour of the series XVIII-XXI in comparison with previously published imidazole derivatives is summarized in [Supplementary Figure S4](#).

The benzothiazole series includes **ISAM-H143** (**176**), a compound exhibiting dual A_{2A}AR/A_{2B}AR antagonist behaviour ($K_i = 90.7$ and 4.30 nM, respectively). This mirrors the behavior of the benzimidazole analogue **ISAM-M89A** ([Fig. 1](#), $K_i = 176$ and 6.10 nM, respectively), which also combines a chlorine atom at position 8 with a 3-furan ring at position 4, suggesting a pattern for further exploration in the rational discovery of A_{2A}AR/A_{2B}AR dual antagonists [[18](#)].

3.5. Enantiospecific binding to A_{2B} and A_{2A}AR

To determine whether the new benzothiazole compounds follow a similar stereospecific recognition pattern, like that recently disclosed for the benzimidazole analogues, three representative ligands were resolved into their enantiopure forms ([Fig. 8A](#)) and evaluated in the four human adenosine receptor subtypes ([Table 9](#)). The selection included two selective A_{2B}AR antagonists (**159** and **161** from series XIX), and the dual A_{2A}AR/A_{2B}AR antagonist **176** from series XXI. These compounds combine promising affinity and selectivity profiles with diverse substitution pattern (i.e., 2- and 3-furyl, 8-Cl and unsubstituted scaffold). A combination of chiral HPLC and circular dichroism (CD) spectroscopy was employed to separate and unequivocally assign the configuration of the stereocenter in each stereoisomer ([Fig. 8A](#)). Semipreparative HPLC separation of (±)-**159**, (±)-**161** and (±)-**176** on a chiral stationary phase (see [Supporting Information](#)) provided the expected six enantiomers with excellent stereochemical purity (>99%). As previously described for structurally related pyrimidine-based derivatives [[10,18–21,47](#)], the characteristic CD activity of the enamide chromophore (300–370 nm) [[48](#)] allowed the unequivocal assignment of the absolute configuration of each enantiomer ([Fig. 8A](#)), by comparison with the reported CD data for enantiopure pyrimidine derivatives of known configuration. At that wavelength, enantiomers showing a negative Cotton effect (dark line) contain the furan ring backward (which corresponds to (S)-**159**, (R)-**161** and (R)-**176**), while the stereoisomers giving positive Cotton effect (light line) contain the pentagonal heterocycle forward (which corresponds to (R)-**159**, (S)-**161** and (S)-**176**). The affinity of the enantiomers of **159**, **161** and **176** was evaluated at the four human adenosine receptors. The results, summarized in [Table 9](#) and [Fig. 8](#) for the four ARs, allow the identification of stereoisomers with excellent A_{2B}AR affinity and selectivity.

The experimental data of benzothiazole derivatives show, for the first time, that both enantiomers can bind to the receptor, albeit favouring the backward enantiomer in all cases in line with the corresponding benzimidazole analogues [[18](#)]. For the A_{2B}AR specific compounds (±)-**159** and (±)-**161** ([Fig. 8B](#), [Table 9](#)), the enantiomer with pentagonal heterocycle backward shows an affinity between 2- and 3-times higher affinity than the racemic mixture, while the other enantiomer shows an affinity 2-fold lower than the racemic mixture. This trend is also observed in the case of the dual A_{2A}AR/A_{2B}AR ligand (**176**). Furthermore, recently reported for the dual A_{2A}AR/A_{2B}AR benzimidazole antagonist [[18](#)], the enantiospecific binding occurs in both A_{2A}AR and A_{2B}AR, also exhibiting higher affinity for the enantiomer with the pentagonal ring backward. The resolution of the racemates has allowed us to obtain two very potent ($K_i < 5$ nM) and selective (>1000 fold) ligands for A_{2B}AR: (S)-**ISAM-MM42** and (R)-**ISAM-MM44** and a new ligand with an excellent A_{2A}AR/A_{2B}AR dual profile [(R)-**ISAM-H143**; $K_i = 27.3$ and 1.20 nM for A_{2A}AR and A_{2B}AR respectively].

The structural and energetic interpretation of those experimental data was investigated through FEP simulation for two pairs of enantiomers with dual A_{2A}AR/A_{2B}AR profile: the new compound **ISAM-H143**, showing a low stereoselectivity, and the previously published compound **ISAM-M89A** [[18](#)], with a high stereoselective profile. Calculations

performed in both the reference solvated state and on our binding model to the hA_{2B}AR, consistently indicated higher affinity for the enantiomer with pentagonal heterocycle oriented backward, that is looking towards TM6 ([Fig. 8B](#)), as previously reported for the former series [[10,18–21,47](#)]. Interestingly, the model shows sensitivity to the lower stereoselectivity of the benzothiazole derivatives, with a smaller energy gap between isomers ($\Delta\Delta G_{\text{bind}} = 2.67 \pm 0.9$ kcal/mol), as compared to the benzimidazole **ISAM-M89A**, ($\Delta\Delta G_{\text{bind}} = 4.65 \pm 1.0$ kcal/mol). In both cases, the simulations show a high degree of convergence, with low SEM and hysteresis values of 0.12 and 1.19 Kcal/mol, respectively.

3.6. Evaluation of the antiproliferative effects

Three representative ligands, the two selective A_{2B}AR antagonists **159** and **164** and the dual A_{2A}AR/A_{2B}AR ligand **176**, were selected for evaluation of the effect on cell proliferation in colorectal cancer cultures ([Fig. 9A](#)). The antiproliferative effects of the novel antagonists followed procedures that recently showed the moderate effect of **ISAM-140** [[49](#)]. As a preliminary step, we evaluated the gene expression of A_{2A}AR and A_{2B}AR in HCT116 human colorectal cancer cells and in primary human CAFs (cancer associated fibroblasts) to investigate the possible different effects of the selective and dual antagonists, between tumor cells and other non-tumoral cells of the tumor microenvironment (TME). As depicted in [Fig. 9B](#), the expression of A_{2B}AR is higher than A_{2A}AR in both cell types, with comparable expression levels in both cancer cell line and CAFs, while A_{2A}AR is differentially expressed between both cell lines, with cancer cells showing an 8-fold increased expression as compared to CAFs.

HCT116 cell proliferation is reduced in a dose-dependent manner upon treatment with the three antagonists, following administration of one single dose of concentrations ranging from 2.5 to 10 μM , both at 24 and 48 hours ([Fig. 9C](#)). Among the three evaluated ligands, the dual **176** shows the highest reduction in cell proliferation, followed by **159**, with 45% and 34% tumor cell proliferation reduction at 48 hours with the highest dose (10 μM), respectively, as compared to the control. None of the selective A_{2B}AR antagonists affect CAFs at any of the concentrations tested, both at 24 and 48 h. However, **176** slightly inhibits cell proliferation in CAFs at the two highest doses (9% of proliferation reduction). The observed effect on non-tumoral cells within the tumor microenvironment, as well as and the big differences observed in cancer cells, between the dual and selective A_{2B}AR antagonists, can be attributed to the expression of both A_{2A}AR and A_{2B}AR, albeit at lower levels. Encouraged by the positive results, we decided to validate these results on a more relevant system, a primary colorectal cancer cell line, using the same type of experiments ([Fig. 9D](#)). Here, all ligands showed a reduction in cell proliferation, although less marked than HCT116 cells, which could be attributed to the slower proliferation rate in primary colorectal cancer cells.

We then moved on to examine the effects of multiple-dose treatment with the antagonists, using three consecutive doses separated by 24 h ([Fig. 9E](#)), and observed a significant enhancement in the overall effect. At 10 μM , compound **159** leads to a 50% reduction in cell proliferation, while the dual antagonist compound **176** demonstrates an even more substantial reduction of 78%. However, it is important to note that the increased antiproliferative efficacy on tumor cells of the last compound comes accompanied by similarly increased effects over CAFs. Thus, although if **176** appears to be the most effective treatment, the selective effect observed for **159** makes it a more promising molecule for the treatment of colorectal cancer.

The reduced cell viability observed upon treatment can be explained either by a direct induction of apoptosis in cancer cells, either through a slowdown of cell cycle dynamics, or both mechanisms happening simultaneously. To deepen into this, we explored these mechanisms by checking apoptosis and cell cycle markers 48 hours after treatment with 10 μM of each selected antagonist. As a readout of cell cycle dynamics, we used the EdU incorporation assay, which measures the number of

cells in S-phase. We observed that both the selective **159** and the dual antagonist **176** exhibited a comparable reduction in cell division (Fig. 9F), whereas $A_{2B}AR$ antagonist **164** had the smallest effect, in line with the results of the proliferation assays. Importantly, none of the antagonists impacted the amount of CAFs in S-phase, with no differences between the antagonist-treated and the control. On the other hand, to identify cells undergoing apoptosis after treatments, we stained cells for Cleaved caspase-3 (CC3), an activated form of caspase-3, involved in the proteolytic cleavage of various cellular substrates, leading to the dismantling of the structural components of the cell and DNA fragmentation. As observed in Fig. 9G, there is a significant increase in the number of apoptotic HCT116 cells upon treatment with antagonists **159** and **176** while no effect was not observed in CAFs. Consistent with all previous assays, compound **164** does not exhibit a significant difference compared to the control. A representative selection of the images taken with confocal microscopy is shown in Supplementary Figure S5.

4. Conclusion

A systematic and highly exploratory approach has been applied to assess new chemical space around the mono-, bi- and tricyclic 3,4-dihydropyrimidin-2(1H)-one chemotypes as $A_{2B}AR$ antagonists. The synthetic accessibility provided by the Biginelli reaction enabled the exploration of up to twenty-three novel scaffolds, with the entire collection of 168 compounds pharmacologically evaluated across the four adenosine receptors. Interpretation of the affinity data through molecular modeling clarified observed SAR trends and highlighted structural determinants for high affinity. Several new ligands combining remarkable affinity ($K_i < 50$ nM) with excellent selectivity were identified, and the antagonistic behaviour was confirmed in functional experiments for a representative selection of fifteen $A_{2B}AR$ selective and a dual $A_{2A}AR/A_{2B}AR$ compound. A joint analysis of the current and previous series, including QM and FEP computational simulations, allowed the establishment of a robust SAR within the series and reinforced the stereoselective binding mode early proposed for this family of $A_{2B}AR$ antagonists. A combination of chiral HPLC and circular dichroism provides experimental support to the modelled stereospecific interaction between the most attractive ligands (**159**, **161** and **176**), and the human $A_{2B}AR$, but also support a stereospecific interaction between **176** and the human $A_{2A}AR$, marking the first observation of measurable affinity in the distomer. *In vitro* evaluation of representative and structurally diverse compounds (**159**, **164** and **176**) in colorectal cancer cell cultures has demonstrated their significant antiproliferative effects by decreasing cell division and increasing apoptosis. The selective impact of the tested antagonists on cancer cells, without affecting CAFs, highlights their potential as promising therapeutic candidates for the treatment of colorectal cancer.

CRediT authorship contribution statement

Rubén Prieto-Díaz: Investigation, Validation, Data curation, Writing – original draft. **Hugo Fojo-Carballo:** Investigation, Methodology, Validation. **Maria Majellaro:** Investigation; Validation; Supervision. Writing – review & editing. **Tana Tandarić:** Investigation, Methodology. **Jhonny Azuaje:** Methodology, Investigation, Validation, Supervision. **José Brea:** Investigation, Formal analysis, Data curation. Writing – review & editing. **Maria I. Loza:** Investigation, Formal analysis, Supervision. **Jorge Barbazán:** Methodology, Investigation, Supervision, Writing – review & editing. **Gloria Salort:** Investigation, Formal analysis, Data curation. **Meera Chotalia:** Investigation, Methodology, Validation. **Iván Rodríguez-Pampín:** Investigation, Methodology, Validation. **Ana Mallo-Abreu:** Investigation, Formal analysis, Validation. **M. Rita Paleo:** Methodology, Investigation, Validation, Supervision. **Xerardo García-Mera:** Methodology, Validation, Supervision. **Francisco Ciruela:** Methodology, Investigation, Supervision, Writing – review & editing. **Hugo Gutierrez-de-Terán:** Methodology,

Investigation, Validation, Supervision, Writing – review & editing. **Eddy Sotelo:** Conceptualization, Methodology, Supervision, Funding acquisition, Writing – original draft, Writing – review & editing.

Declaration of Competing Interest

The authors declare the following financial interests/personal relationships which may be considered as potential competing interests: EDDY SOTELO reports was provided by Government of Galicia.

Data availability

No data was used for the research described in the article.

Acknowledgements

This work was financially supported by the Consellería de Cultura, Educación e Ordenación Universitaria of the Galician Government: (grant: ED431B 2020/43, EDAC431C 2022/20, ED431B 2023/23), Centro Singular de Investigación de Galicia accreditation 2019–2022 (ED431G 2019/03) and the European Regional Development Fund (ERDF), Ministerio de Ciencia e Innovación – Agencia Estatal de Investigación-FEDER-UE (PID2020–118511RB-I00 and PID2021–1240100B-100). The computations were performed on resources provided by the Swedish National Infrastructure for Computing (SNIC). Additional support is acknowledged from the Swedish strategic research program eSENCE, Xunta de Galicia (ED431C 2018/21 and ED431G 2019/02) and European Regional Development Fund (ERDF) in the frame of the Recovery Assistance for Cohesion and the Territories of Europe (REACT-EU) funds. GS received a Margarita Salas fellowship from the Ministerio de Universidades and funded by the European Union-NextGenerationEU. This research program has been developed in the frame of the European COST action ERNEST (CA 18133).

Supporting Information

Experimental details of the synthesis and characterization of all compounds described. Molecular formula strings. Chiral HPLC chromatograms for enantiomers and racemic mixtures. HPLC chromatograms for purity analysis of representative compounds. Homology models: Authors will release the atomic coordinates upon article publication. The Supporting Information is available free of charge on the website.

Appendix A. Supporting information

Supplementary data associated with this article can be found in the online version at doi:10.1016/j.biopha.2024.116345.

References

- [1] B.B. Fredholm, Adenosine - A physiological or pathophysiological agent? *J. Mol. Med.* 92 (2014) 201–206, <https://doi.org/10.1007/s00109-013-1101-6>.
- [2] K.A. Jacobson, Z.-G. Gao, Adenosine receptors as therapeutic targets, *Nat. Rev. Drug Discov.* 5 (2006) 247–264, <https://doi.org/10.1038/nrd1983>.
- [3] J.F. Chen, H.K. Eltzschig, B.B. Fredholm, Adenosine receptors as drug targets-what are the challenges? *Nat. Rev. Drug Discov.* 12 (2013) 265–286, <https://doi.org/10.1038/nrd3955>.
- [4] C.M. Aherne, E.M. Kewley, H.K. Eltzschig, The resurgence of A2B adenosine receptor signaling, *Biochim. Biophys. Acta - Biomembr.* 1808 (2011) 1329–1339, <https://doi.org/10.1016/j.bbame.2010.05.016>.
- [5] B.B. Fredholm, Adenosine, an endogenous distress signal, modulates tissue damage and repair, *Cell Death Differ.* 14 (2007) 1315–1323, <https://doi.org/10.1038/sj.cdd.4402132>.
- [6] B.B. Fredholm, A.P. IJzerman, K.A. Jacobson, J. Linden, C.E. Müller, International union of basic and clinical pharmacology. LXXXI. Nomenclature and classification of adenosine receptors - An update, *Pharmacol. Rev.* 63 (2011) 1–34, <https://doi.org/10.1124/pr.110.003285>.

- [7] C.N. Wilson, M.S. Jamal, Adenosine Receptors in Health and Disease, in: *Handb. Exp. Pharmacol.*, 1st ed., Springer, Berlin, 2009, pp. 41–75, <https://doi.org/10.1016/B978-0-12-385526-8.00002-3>.
- [8] A.Huiri, R. Prieto-Díaz, S. Neo, L. Tong, X. Chen, V. Carannante, B. Önfelt, J. Hartman, F. Haglund, M. Majellaro, J. Azuaje, X. García-Mera, J.M. Brea, M. I. Loza, W. Jespers, H. Gutiérrez-De-Terán, E. Sotelo, A. Lundqvist, A2B adenosine receptor antagonists rescue lymphocyte activity in adenosine-producing patient-derived cancer models, 4592–4592, *J. Immunother. Cancer* 10 (2022), <https://doi.org/10.1136/jitc-2022-004592>.
- [9] D. Allard, M. Turcotte, J. Stagg, Targeting A2 adenosine receptors in cancer, *Immunol. Cell Biol.* 95 (2017) 333–339, <https://doi.org/10.1038/icb.2017.8>.
- [10] M. Majellaro, W. Jespers, A. Crespo, M. Nunez, S. Novio, J. Azuaje, R. Prieto-Díaz, C. Gioe, B. Alispahic, J. Brea, M. Loza, M. Freire-Garabal, C. García-Santiago, C. Rodríguez-García, X. García-Mera, O. Caamaño, C.F. Masaguer, F.J. Sardina, E. Stefanachi, A. El Maatougui, A. Mallo-Abreu, J. Åqvist, H. Gutiérrez-de-Terán, E. Sotelo, 3,4-Dihydropyrimidin-2(1H)-ones as Antagonists of the Human A2B Adenosine Receptor: Optimization, Structure–Activity Relationship Studies, and Enantiospecific Recognition, *J. Med. Chem.* 64 (2021) 458–480, <https://doi.org/10.1021/acs.jmedchem.0c01431>.
- [11] R. Franco, R. Rivas-Santisteban, G. Navarro, I. Reyes-Resina, Adenosine receptor antagonists to combat cancer and to boost anti-cancer chemotherapy and immunotherapy, *Cells* 10 (2021) 2831–2844, <https://doi.org/10.3390/cells10112831>.
- [12] S. Hinz, G. Navarro, D. Borroto-Escuela, B.F. Seibt, Y.-C. Ammon, E. de Filippo, A. Danish, S.K. Lacher, B. Červinková, M. Rafehi, K. Fuxe, A.C. Schiedel, R. Franco, C.E. Müller, Adenosine A2A receptor ligand recognition and signaling is blocked by A2B receptors, *Oncotarget* 9 (2018) 13593–13611, <https://doi.org/10.18632/oncotarget.24423>.
- [13] J. Jiang, C.J. Seel, A. Temirak, V. Namasivayam, A. Arridu, J. Schabikowski, Y. Baqi, S. Hinz, J. Hockemeyer, C.E. Müller, A2B Adenosine Receptor Antagonists with Picomolar Potency, *J. Med. Chem.* 62 (2019) 4032–4055, <https://doi.org/10.1021/acs.jmedchem.9b00071>.
- [14] M. Stewart, A.G. Steinig, C. Ma, J.-P. Song, B. McKibben, A.L. Castelhanos, S. J. MacLennan, 3HJOSIP339391, a selective, novel, and high affinity antagonist radioligand for adenosine A2B receptors, *Biochem. Pharmacol.* 68 (2004) 305–312, <https://doi.org/10.1016/j.bcp.2004.03.026>.
- [15] R.V. Kalla, E. Elzein, T. Perry, X. Li, A. Gimbel, M. Yang, D. Zeng, J. Zablocki, Selective, high affinity A2B adenosine receptor antagonists: N-1 monosubstituted 8-(pyrazol-4-yl)xanthines, *Bioorg. Med. Chem. Lett.* 18 (2008) 1397–1401, <https://doi.org/10.1016/j.bmcl.2008.01.008>.
- [16] A. Crespo, A. El Maatougui, P. Biagini, J. Azuaje, A. Coelho, J. Brea, M.I. Loza, M. I. Cadavid, X. García-Mera, H. Gutiérrez-De-Terán, E. Sotelo, Discovery of 3,4-dihydropyrimidin-2(1H)-ones as a novel class of potent and selective A2B adenosine receptor antagonists, *ACS Med. Chem. Lett.* 4 (2013) 1031–1036, <https://doi.org/10.1021/ml400185v>.
- [17] A. El Maatougui, J. Azuaje, M. González-Gómez, G. Miguez, A. Crespo, C. Carbajales, L. Escalante, X. García-Mera, H. Gutiérrez-De-Terán, E. Sotelo, Discovery of Potent and Highly Selective A2B Adenosine Receptor Antagonist Chemotypes, *J. Med. Chem.* 59 (2016) 1967–1983, <https://doi.org/10.1021/acs.jmedchem.5b01586>.
- [18] R. Prieto-Díaz, M. González-Gómez, H. Fojo-Carballo, J. Azuaje, A. El Maatougui, M. Majellaro, M.I. Loza, J. Brea, V. Fernández-Dueñas, M.R. Paleo, A. Díaz-Holgún, B. García-Pinel, A. Mallo-Abreu, J.C. Estévez, A. Andújar-Arias, X. García-Mera, I. Gomez-Tourino, F. Ciruela, C.O. Salas, H. Gutiérrez-de-Terán, E. Sotelo, Exploring the Effect of Halogenation in a Series of Potent and Selective A2B Adenosine Receptor Antagonists, *J. Med. Chem.* 66 (2023) 890–912, <https://doi.org/10.1021/acs.jmedchem.2c01768>.
- [19] A. Mallo-Abreu, R. Prieto-Díaz, W. Jespers, J. Azuaje, M. Majellaro, C. Velando, X. García-Mera, O. Caamaño, J. Brea, M.I. Loza, H. Gutiérrez-De-Terán, E. Sotelo, Nitrogen-Walk Approach to Explore Bioisosteric Replacements in a Series of Potent A2B Adenosine Receptor Antagonists, *J. Med. Chem.* 63 (2020) 7721–7739, <https://doi.org/10.1021/acs.jmedchem.0c00564>.
- [20] A. Mallo-Abreu, M. Majellaro, W. Jespers, J. Azuaje, O. Caamaño, X. García-Mera, J.M. Brea, M.I. Loza, H. Gutiérrez-De-Terán, E. Sotelo, Trifluorinated Pyrimidine-Based A2B Antagonists: Optimization and Evidence of Stereospecific Recognition, *J. Med. Chem.* 62 (2019) 9315–9330, <https://doi.org/10.1021/acs.jmedchem.9b01340>.
- [21] C. Carbajales, J. Azuaje, A. Oliveira, M.I. Loza, J. Brea, M.I. Cadavid, C. F. Masaguer, X. García-Mera, H. Gutiérrez-De-Terán, E. Sotelo, Enantiospecific Recognition at the A2B Adenosine Receptor by Alkyl 2-Cyanoimino-4-substituted-6-methyl-1,2,3,4-tetrahydropyrimidin-5-carboxylates, *J. Med. Chem.* 60 (2017) 3372–3382, <https://doi.org/10.1021/acs.jmedchem.7b00138>.
- [22] J. Taura, V. Fernández-Dueñas, F. Ciruela, Determination of GPCR-Mediated cAMP Accumulation in Rat Striatal Synaptosomes, in: R. Luján, F. Ciruela (Eds.), *Recept. Ion Channel Detect. Brain Methods Protoc.*, Springer, New York, NY, 2016, pp. 455–463, https://doi.org/10.1007/978-1-4939-3064-7_28.
- [23] P. Leff, I.G. Dougall, Further concerns over Cheng-Prusoff analysis, *Trends Pharmacol. Sci.* 14 (1993) 110–112, [https://doi.org/10.1016/0165-6147\(93\)90080-4](https://doi.org/10.1016/0165-6147(93)90080-4).
- [24] H.J. Motulsky, R.E. Brown, Detecting outliers when fitting data with nonlinear regression – a new method based on robust nonlinear regression and the false discovery rate, 123–123, *BMC Bioinforma.* 7 (2006), <https://doi.org/10.1186/1471-2105-7-123>.
- [25] H. Gutiérrez-De-Terán, X. Bello, D. Rodríguez, Characterization of the dynamic events of GPCRs by automated computational simulations, in: Portland Press,, 2013, pp. 205–212, <https://doi.org/10.1042/BST20120287>.
- [26] C. Lu, C. Wu, D. Ghoreishi, W. Chen, L. Wang, W. Damm, G.A. Ross, M.K. Dahlgren, E. Russell, C.D. Von Bargen, R. Abel, R.A. Friesner, E.D. Harder, OPLS4: Improving force field accuracy on challenging regimes of chemical space, *J. Chem. Theory Comput.* 17 (2021) 4291–4300, <https://doi.org/10.1021/acs.jctc.1c00302>.
- [27] T.A. Halgren, R.B. Murphy, R.A. Friesner, H.S. Beard, L.L. Frye, W.T. Pollard, J. L. Banks, Glide: A New Approach for Rapid, Accurate Docking and Scoring. 2. Enrichment Factors in Database Screening, *J. Med. Chem.* 47 (2004) 1750–1759, <https://doi.org/10.1021/jm030644s>.
- [28] J. Marelus, K. Kolmodin, I. Feierberg, J. Åqvist, Q: A molecular dynamics program for free energy calculations and empirical valence bond simulations in biomolecular systems, *J. Mol. Graph. Model.* 16 (1998) 213–225, [https://doi.org/10.1016/S1093-3263\(99\)00012-1](https://doi.org/10.1016/S1093-3263(99)00012-1).
- [29] W. Jespers, M. Esguerra, J. Åqvist, H. Gutiérrez-De-Terán, Qligfep: An automated workflow for small molecule free energy calculations in Q, *J. Chem. Inf. Model.* 11 (2019) 1–16, <https://doi.org/10.1186/s13321-019-0348-5>.
- [30] G. King, A. Warshel, A surface constrained all-atom solvent model for effective simulations of polar solutions, *J. Chem. Phys.* 91 (1989) 3647–3661, <https://doi.org/10.1063/1.456845>.
- [31] F.S. Lee, A. Warshel, A local reaction field method for fast evaluation of long-range electrostatic interactions in molecular simulations, *J. Chem. Phys.* 97 (1992) 3100–3107, <https://doi.org/10.1063/1.462997>.
- [32] J.-P.J.P. Ryckaert, G. Ciccotti, H.J.C.H. Berendsen, Numerical integration of the cartesian equations of motion of a system with constraints: molecular dynamics of n-alkanes, *J. Comput. Phys.* 23 (1977) 327–341, [https://doi.org/10.1016/0021-9991\(77\)90098-5](https://doi.org/10.1016/0021-9991(77)90098-5).
- [33] M.J. Robertson, J. Tirado-Rives, W.L. Jorgensen, Improved Peptide and Protein Torsional Energetics with the OPLS-AA Force Field, *J. Chem. Theory Comput.* 11 (2015) 3499–3509, <https://doi.org/10.1021/acs.jctc.5b00356>.
- [34] O. Berger, O. Edholm, F. Jähnig, Molecular dynamics simulations of a fluid bilayer of dipalmitoylphosphatidylcholine at full hydration, constant pressure, and constant temperature, *Biophys. J.* 72 (1997) 2002–2013, [https://doi.org/10.1016/S0006-3495\(97\)78845-3](https://doi.org/10.1016/S0006-3495(97)78845-3).
- [35] C.H. Bennett, Efficient estimation of free energy differences from Monte Carlo data, *J. Comput. Phys.* 22 (1976) 245–268, [https://doi.org/10.1016/0021-9991\(76\)90078-4](https://doi.org/10.1016/0021-9991(76)90078-4).
- [36] S. Sastre, R. Casanovas, F. Muñoz, J. Frau, Isodesmic reaction for accurate theoretical pKa calculations of amino acids and peptides, *Phys. Chem. Chem. Phys.* 18 (2016) 11202–11212, <https://doi.org/10.1039/C5CP07053H>.
- [37] J. Ho, M.L. Coote, pKa Calculation of Some Biologically Important Carbon Acids - An Assessment of Contemporary Theoretical Procedures, *J. Chem. Theory Comput.* 5 (2009) 295–306, <https://doi.org/10.1021/ct800335v>.
- [38] R. Casanovas, J. Ortega-Castro, J. Frau, J. Donoso, F. Muñoz, Theoretical pKa calculations with continuum model solvents, alternative protocols to thermodynamic cycles, *Int. J. Quantum Chem.* 114 (2014) 1350–1363, <https://doi.org/10.1002/qua.24699>.
- [39] J. Ho, M.L. Coote, A universal approach for continuum solvent pKa calculations: are we there yet? *Theor. Chem. Acc.* 125 (2010) 3–21, <https://doi.org/10.1007/s00214-009-0667-0>.
- [40] A.V. Marenich, C.J. Cramer, D.G. Truhlar, Universal Solvation Model Based on Solute Electron Density and on a Continuum Model of the Solvent Defined by the Bulk Dielectric Constant and Atomic Surface Tensions, *J. Phys. Chem. B* 113 (2009) 6378–6396, <https://doi.org/10.1021/jp810292n>.
- [41] M. ea Frisch, G. Trucks, H.B. Schlegel, G. Scuseria, M. Robb, J. Cheeseman, G. Scalmani, V. Barone, G. Petersson, H. Nakatsuji, Gaussian 16, revision C.01, (2016).
- [42] A. Glentis, P. Oertle, P. Mariani, A. Chikina, F. El Marjoui, Y. Attieh, F. Zaccarini, M. Lae, D. Loew, F. Dingli, P. Sirven, M. Schoumacher, B.G. Gurchenkov, M. Plodinec, D.M. Vignjevic, Cancer-associated fibroblasts induce metalloprotease-independent cancer cell invasion of the basement membrane, 924–924, *Nat. Commun.* 8 (2017), <https://doi.org/10.1038/s41467-017-00985-8>.
- [43] J. Barbazan, C. Pérez-González, M. Gómez-González, M. Dedenon, S. Richon, E. Latorre, M. Serra, P. Mariani, S. Descroix, P. Sens, X. Trepas, D.M. Vignjevic, Cancer-associated fibroblasts actively compress cancer cells and modulate mechanotransduction, *bioRxiv* (2021) 2021.04.05.438443-2021.04.05.438443, (<https://doi.org/10.1101/2021.04.05.438443>).
- [44] RDKit. (<https://www.rdkit.org>).
- [45] Schrödinger Release 2022-4: Maestro, Schrödinger, (2022).
- [46] Y. Chen, J. Zhang, Y. Weng, Y. Xu, W. Lu, W. Liu, M. Liu, T. Hua, G. Song, Cryo-EM structure of the human adenosine A2B receptor–Gs signaling complex, *Sci. Adv.* 8 (n.d.) eadd3709. (<https://doi.org/10.1126/sciadv.add3709>).
- [47] X. Wang, W. Jespers, R. Prieto-Díaz, M. Majellaro, A.P. IJzerman, G.J.P.P. van Westen, E. Sotelo, L.H. Heitman, H. Gutiérrez-de-Terán, Identification of V6.51L as a selectivity hotspot in stereoselective A2B adenosine receptor antagonist recognition, *Sci. Rep.* 11 (2021) 1–10, <https://doi.org/10.1038/s41598-021-93419-x>.
- [48] W. Krenn, P. Verdino, G. Uray, K. Faber, C.O. Kappe, Determination of absolute configuration in 4-aryl-3, 4-dihydro-2(1H)-pyrimidones by high performance liquid chromatography and CD spectroscopy, *Chirality* 11 (1999) 659–662, [https://doi.org/10.1002/\(SICI\)1520-636X\(1999\)11:8<659::AID-CHIR8>3.0.CO;2-V](https://doi.org/10.1002/(SICI)1520-636X(1999)11:8<659::AID-CHIR8>3.0.CO;2-V).
- [49] J. Barbazan, M. Majellaro, A.L. Martínez, J.M. Brea, E. Sotelo, M. Abal, Identification of A2BAR as a potential target in colorectal cancer using novel fluorescent GPCR ligands, 113408–113408, *Biomed. Pharmacother.* 153 (2022), <https://doi.org/10.1016/j.biopha.2022.113408>.